Performance improvement of radioisotope thermoelectric generators (RTGs) by design optimization

Stylianos Kyrimis [a,*,1] , Eliott Lallemand [a,b,1], Christian Stiewe [a], Pawel Ziolkowski [a],
Aidan Cowley [b], Eckhard Müller [a], Johannes de Boor [a,*]

[a] *Institute of Materials Research, German Aerospace Centre (DLR), Cologne, Germany*
[b] *European Astronaut Centre (EAC), European Space Agency (ESA), Cologne, Germany*

A B S T R A C T

Lunar exploration requires a continuous supply of electrical power, independent of solar irradiation availability. This can be provided by Radioisotope Thermoelectric Generators (RTG) which have been successfully deployed in various deep-space missions, proving their reliability and longevity. Design and operation of an RTG is a complex multi-disciplinary challenge, as they consist of a multitude of functionally interlinked components. To optimize the system, we developed a thermoelectric network model to rapidly simulate RTG operation. Using an iterative process, our network model calculates the heat flow and the temperature difference across each RTG component and from this evaluates the electrical power generated by the thermoelectric modules. We used the ^{241}Am-based RTG design with Bi_2Te_3-based thermoelectric modules, developed by the European Space Agency, as baseline and coupled our network model to a genetic algorithm to identify an RTG design with maximum specific power while maintaining safe operating temperature limits. The optimized RTG design reaches a specific power of 1.38 W/kg at a power output of 13.9 W$_{el}$ assuming environmental temperatures typical for the lunar surface, a considerable increase over earlier results of 1 W/kg and 10 W$_{el}$. Validation of our tool with a finite element analysis model revealed excellent agreement, with a power output difference of 1.1 % and a three order of magnitude reduction in computational time. Our methodology thus allows for fast but accurate optimization of RTGs, an understanding of the interplay between the different parameters, and the adaptation of RTGs to different environments, accelerating their advancement for future deployment.

1. Introduction

Investment in space research and exploration has yielded a wide range of socioeconomic benefits, such as new science, environmental monitoring, communications and new materials [1]. Moreover, the establishment of a human colony on the Lunar surface, as part of Project Artemis [2], and later on the Martian surface, could act as the foundation for a vibrant space economy based on resource mining or space tourism [3,4]. These prospects have attracted considerable funding increase in both the European Space Agency (ESA), whose budget increased from 4.3B€ in 2013 to 7.79B€ in 2025 [5], as well as in the U.S. National Aeronautics and Space Administration (NASA) whose budget increased from 19B$ in 2017 to over 27B$ in 2024 [6].

Space research missions can be categorized based on their preferential power source. Low-Earth orbit applications or orbital exploration of inner planets, i.e. Mercury, Venus and Mars, have solar irradiation of sufficient intensity to power their activities through photovoltaic cells. However, this is not the case for deep space or surface exploration applications. For these, solar irradiation may be too low in intensity, e.g. missions beyond Jupiter [7], or unavailable for long periods of times, e. g. on the Moon where lunar night lasts 15 Earth days [8]. Moreover, dust accumulation on solar panels, as would be the case with Moon and Mars, quickly degrades the power output as shown in a recent NASA study [9]. To power scientific apparatus in such situations, NASA developed the technology of the Radioisotope Thermoelectric Generator (RTG) as early as mid-1950 s [10]. Several types of RTGs have been developed that powered high-profile missions, such as the SNAP-27 RTG used in the Apollo program, the GPHS-RTG used in Galileo, Ulysses and Cassini missions, and the MMRTG used in the Curiosity and Perseverance rovers [10]. Throughout decades of usage, the RTGs have proven their

---

reliability and longevity, as no mission was terminated prematurely because of RTG failure and most missions exceeded their intended operation lifetime [11]. Recently, ESA started funding the development of its own scalable RTG [12], where each stackable unit aims to produce 10 W$_{el}$ (electrical power output) from a 200 W$_{th}$ (thermal power output) heat source. However, it has not been flight-tested yet.

In its core, the RTG utilizes the heat generated continuously by the radioactive decay of a radioisotope material. In NASA's case, ^{238}Pu was deployed because of its availability in the U.S.A. as a side product of nuclear weapon production [13]. However, with the current legislations against nuclear weapons, ^{238}Pu production has halted and alternative options are being investigated. For ESA, due to the limited availability of ^{238}Pu in Europe, research conducted by the UK's National Nuclear Laboratory has identified ^{241}Am as a potential candidate for RTG systems [12,14]. ^{241}Am is a by-product of the civil nuclear energy industry, produced by the beta decay of ^{241}Pu, thus making it widely available in Europe [14]. Compared to ^{238}Pu, ^{241}Am has a longer half-life, 432.6 years as opposed to 87.7 years, but a lower specific thermal output, 0.1 W/g as opposed to 0.5 W/g [15]. The lower thermal output means that ^{241}Am-based RTGs will have lower specific power by design, i.e. electrical power output per system mass, compared to ^{238}Pu-based RTGs. This is a key aspect as specific power must be maximized to reduce launching costs [16]. Despite this downside, the wider availability of ^{241}Am, its radiation safety (it has a lower radioactivity than ^{238}Pu thus requiring less shielding), lower cost and longer half-life make it one of the best alternatives for the next RTG generations [17,18].

It is key for the utilization of nuclear resources in space to ensure safe containment of the nuclear fuel during all mission phases, including ground handling and launch, as well as during unplanned events such as accidental reentry, impact and post-impact situations [19,20]. Therefore, the inner RTG core utilizes a multilayer architecture. The nuclear fuel is manufactured using a ceramic form, which has low chemical reactivity and high mechanical strength [19]. A metallic cladding surrounds the fuel, which should be impact-resistant, oxidation-resistant, weldable and suitable as a diffusion barrier [20]. In NASA's RTGs, an iridium alloy has been used [21], while in the ESA RTG a Pt-20 %Rh alloy cladding is considered which has been extensively tested for its mechanical strength and oxidation resistance [22,23]. An insulating graphitic foam sleeve is surrounding the clad to protect the fuel and the clad against the extreme temperatures of an accidental re-entry. The loaded sleeves are then placed within an aeroshell containment, which protects the inner components from thermal shocks or ablation during a hypersonic re-entry, while also acting as a thermo-mechanical interface with the outer RTG components [10,12]. This fuel-clad-sleeve-aeroshell assembly is henceforth mentioned as the European Large Heat Source (ELHS) [24].

The radioactive decay heat is partially converted into electricity via thermoelectric (TE) materials. Specifically, *p*- and *n*-type TE materials in the shape of prismatic legs, joined into a multitude of *pn*-couples, are deployed in a TE module (TEM). The *p*- and *n*-type legs in each of the thermocouples are connected electrically in series and thermally in parallel [25]. TEMs utilize the Seebeck effect to convert a heat flow due to a temperature difference into electrical power. The performance of a TEM depends on the TE properties of the deployed materials, in particular on their TE figure of merit *zT*, on the interface properties, and on the geometry of the legs and the module [25,26]. In the RTG, the hot junctions of the TEM are placed close to the radioisotope fuel and, to facilitate a large temperature difference across them, radiative fins are installed at their cold junctions to dissipate the residual heat to the environment.

Over the course of its lifetime, the RTG performance drops for two mains reasons, the natural decay of the fuel's radioactivity and the degradation of the TE modules [27]. The heat released by the radioactive fuel depends on the utilized isotopes' half-life time. The exponential decay of ^{238}Pu is ~0.75 % per year [21], while ^{241}Am decays at a rate of ~0.16 % per year, which amounts to only 2.7 % for a 17-year mission as

is the Mars Science Laboratory (MSL) Curiosity rover. The degradation of the TEM can be categorized into changes of the functional materials, e.g. due to diffusion, sublimation, etc., and of the contacting interfaces, e.g. due to cracking, delamination, diffusion and possible formation of reaction layers [28–31]. Such phenomena are governed by the operating temperature and are therefore usually most pronounced at the hot junction of the TE material, with temperatures above the maximum specified operating temperature having an accelerating impact. Extensive tests on skutterudite-based TEM have been run by NASA to understand the drivers of degradation phenomena and they identified that a metallic coating on the hot TEM junction was very effective at reducing degradation phenomena [32,33]. The RTG structure, i.e. material choice, thickness, shape of employed components and their thermal coupling conditions, determines the magnitude of heat flux at the hot TE junction which then determines the best TE materials choice for deployment. Each TE material type has a temperature range for optimum operation, as well as a maximum operating temperature that should not be exceeded to prevent structural damage or material degradation [34]. Throughout the different generations of RTGs, several TE materials have been deployed, such as SiGe (GPHS-RTG), PbTe/ TAGS-85 (MMRTG) and Bi$_2$Te$_3$ (ESA-RTG) [10,12]. Radiation from the radioactive decay or from a cosmic origin, e.g. solar storms, can damage the TEM, altering its TE properties. The heritage TEMs used by NASA have proven their resistance to radiation damage, as their operation exceeded their intended mission scenario by far. While the Bi$_2$Te$_3$ module deployed in the ESA RTG has not been flight tested yet, its radiation resistance has been experimentally verified [35]. Unlike NASA's RTG that usually follow a polygonal design, the ELHS has a truncated triangle cross section, with TEMs placed at the short edges and thermal insulation on the long edges, as well as at the base and top faces of the RTG. Here, six radiative fins are installed per RTG unit [12]. As RTGs are intended for deep-space environments or for surface exploration where natural convection is absent, cooling through thermal radiation from the fins into the cold environment is the predominant temperature control method. Consequently, larger fin surface area translates to higher cooling efficiency, and thus higher power output, however the overall system mass also increases, reducing the RTG's specific power. Optimization of RTGs is therefore a delicate balance of nuclear fuel choice, component material selection, structural design for efficient heat transfer, and suitability and performance of the TEMs, with the specific power and the safe operating temperature limits being the key optimization drivers.

Such a systematic optimization of the RTG technology requires multi-parametric tools that are able to analyze the RTG behavior and performance in-depth under realistic mission scenarios. For this, Finite Element Analysis (FEA) modelling has been used. For the MMRTG, Barklay *et al.* [36] and Whiting *et al.* [37] performed thermal simulations to investigate design modifications. Barklay *et al.* [36] considered installing additional TEMs internally, i.e. within the MMRTG housing, or externally, i.e. between the housing and the fins, as well as changing the fin number and dimensions. The FEA simulations revealed that the external TEM configuration performed the best, increasing the power output by up to 22 %, but all modifications considerably reduced the specific power compared to the baseline design. Whiting *et al.* [37] investigated the MMRTG behavior when operating it at different voltages, i.e. 28 V (nominal operation) and 32 V, and accounting for the lunar day and night conditions as thermal boundary conditions. It was found that higher voltage operation leads to elevated internal temperatures at the TEM which could cause structural damage, although the driving factors of these phenomena were not explored. For the ESA RTG, Ambrosi *et al.* [12] performed thermal simulations focusing on analyzing the temperature and heat distribution to ensure compliance with material temperature limits in the current geometry, however system optimization was not considered. Barco *et al.* utilized mechanical simulations focusing solely on impact modelling to test the stability of the fuel assembly during accident scenarios, confirming that the current

encapsulation strategies can prevent fuel leakage [23,38]. These studies primarily focused on purely thermal or mechanical simulations, treating the TEM as a passive, conductive element. In fact, 3D FEA TE simulations for RTG investigations have only recently appeared in the literature. Tailin *et al.* investigated the performance of the Chinese Chang'E-4 RTG during its lunar operation [39]. They identified that according to its position with respect to the sun, different temperatures at the TEM and RTG components were observed [39]. Liu *et al.* simulated the MMRTG and investigated its behavior during operation, observing a non-uniform lateral temperature distribution at the hot TEM junction [40]. To the best of our knowledge, 3D FEA TE simulations for the ESA RTG have not yet appeared in the literature.

Full TE simulations are a highly valuable tool to optimize and advance the technology readiness level (TRL) of the RTG. They provide valuable insight into the 3D heat flux distribution within the various RTG components and link it to the operating regime of the TEMs, guiding decisions for safe operation strategies during mission scenarios. This approach is highly beneficial due to the difficulty in obtaining data from RTG hardware under operation, given the vast cost and effort for a test in space or even in laboratory conditions as nuclear protocols are quite strict, thus limiting laboratory investigations to electrical analogues [34,38]. The scarcity of TE simulations in literature therefore forms a considerable barrier for timely development of optimized RTGs. On the other hand, while 3D FEA simulations yield valuable data for the in-depth analysis of the RTG behavior, they are restricted by their large computational resource demands, making them a time-consuming and expensive tool for the extensive multi-parametric investigations necessary when design optimization is considered. Consequently, there is a need for a method to model the TE performance of the RTG system that is orders of magnitude faster in computation time compared to FEA, whilst keeping a high level of accuracy. TEMs are often represented by (coupled) electrical and thermal network models, with network elements mimicking the ceramic housing, the TE legs and the interconnecting electrical bridges, to calculate the temperature profiles across all components and use it to evaluate the TE performance by solving the TE heat transfer equation [41–44]. By comparing these predictions with experimental results, the influence of unaccounted-for phenomena, e.g. degrading interface resistances or large drops in performance due to crack formation, can be assessed [42,45]. Then, expanding such network models to also include additional heat transfer components can enable a detailed investigation on the system level. Examples of such studies include the coupling of TEMs with heat exchangers to recover heat from exhaust gases [46], with a solar absorber to model a solar thermoelectric generator system [47] and with an infrared radiative cooler within a radiative cooling based TE device [48]. Consequently, introducing a similar TE network model to approach the RTG system as a circuit of thermal and thermoelectric resistances could allow for a rapid performance estimation tool that could be deployed for design optimization.

An example of this is the study of Jing *et al.* [49], who developed a model of a mW-scale RTG powered by PuO_2 fuel and using a Skutterudite-based TEM. The RTG was modelled as a purely thermal resistance model, consisting of heat source and sink as well as several resistors to account for TEM, insulation, etc. It considered two heat paths for the radioactive decay heat, one across the TEM and the other along a parasitic bypass. This network model was employed to analyze the influence of key TEM parameters (the number, the length and the cross-sectional area of the TE legs) on the heat and temperature distribution in the RTG; a few specific configurations were also modeled using coupled TE and mechanical simulations with 3D FEA. The authors used several approximations for their network model, specifically assuming constant TE material properties and open circuit conditions, neglecting current-related terms such as the considerable influence of Peltier heat flow on temperature distribution and TEM performance. Furthermore, they did not validate their network model against FEA results.

A similar approach was used in Mesalam *et al.* [24] who introduced

Stirling convertors on the ELHS instead of TEMs. They employed a thermal resistance network model to approach the system and investigated the influence of parameters such as fin length, convertor stroke and convertor failure on the system performance [24]. Stirling-based radioisotope power systems are currently investigated by both NASA and ESA as a potential alternative to RTGs, as they can reach higher specific power [24,50–52]. However, while Stirling-based radioisotope power systems have yet to be flight tested, RTGs have consistently demonstrated long-term reliability in space missions, making them a critical component of ESA's technology 2040 roadmap [53]. As such, improving RTG specific power remains a critical area of investigation.

In this paper, we address the need for a rapid multi-parametric model with fully incorporated TE phenomena, suitable for RTG design optimizations. We present a TE network model (NM) which approximates the RTG components, except for the TEM, as a series of thermally conductive or radiative elements. The heat released by the fuel is distributed along two paths, the heat flowing through the TEM branch, $\dot{Q}_{TEM-In}$, and the parasitic heat flow that passes through the insulation, $\dot{Q}_{By}$. Through an iterative process, the temperature distribution within each RTG component can be calculated based on these heat flows. This is then used to solve the TE heat transfer equation for the TEM and identify the optimum current and maximum power output. The TE NM is combined with a genetic algorithm (GA) to perform a detailed parametric study to identify the RTG design which maximizes the specific power without exceeding the safe operation temperature limits of the hot side TEM junction and of the protective cladding. To verify the TE NM, the results of the optimized RTG geometry were compared to those of a 3D FEA TE model, showcasing excellent accuracy and a considerable reduction in the required computational resources. The structure of the model and the underlying equations describing the thermal and TE effects are presented here in detail.

2. Models and methods

2.1. Geometry of the ESA RTG

Throughout this study, we consider a single RTG unit, consisting of one ELHS surrounded by all components that make up the RTG, such as insulation, hull and TEM. Situations that would require multiple ELHS and RTG units to be stacked together to increase the power output will introduce some modifications to the design of each unit that will be mentioned when necessary. The ELHS currently under development by ESA contains a 200 W_{th} radioisotope heat source, composed of 12 fuel pellets, enclosed in a Pt-Rh cladding and surrounded by a graphitic foam sleeve, which are all placed within a carbon–carbon composite aeroshell [12]. The assembly of the ELHS is presented in Fig. 1a. The fuel pellets are cylinders with a diameter of 27 mm and a height of 35 mm. The thickness of the clads and sleeves are not specified in the literature, but are estimated to be around 2–3 mm [23], while the final dimensions of the aeroshell core are a short-side length of 49 mm, a long-side length of 117 mm and a height of 113 mm [12].

One of the requirements of the developed model is to provide a versatile code that can be used with several designs and various geometrical parameters. To fulfill this while keeping the code accurate, computationally efficient and user-friendly, the RTG geometry is broken down into a handful of interrelated parameters. The number and dimensions of the ^{241}Am pellets, which are defined by their diameter, D_{Am}, and height, h_{Am}, as used by Ambrosi *et al.* [12], form the basis of the RTG design. The cladding and sleeves retain the cylindrical form and have a constant thickness, referred to as t_{clad}, and t_{sleeve}, respectively. To simplify the complex prismatic truncated triangle shape of the ELHS, the six cylindrical sleeves are assumed to be packed as closely as possible in the center of the aeroshell structure. This allows us to approximate them as a pseudo-volume with the shape of an inner truncated triangle, depicted with the dashed lines in Fig. 1b, which can be expressed with
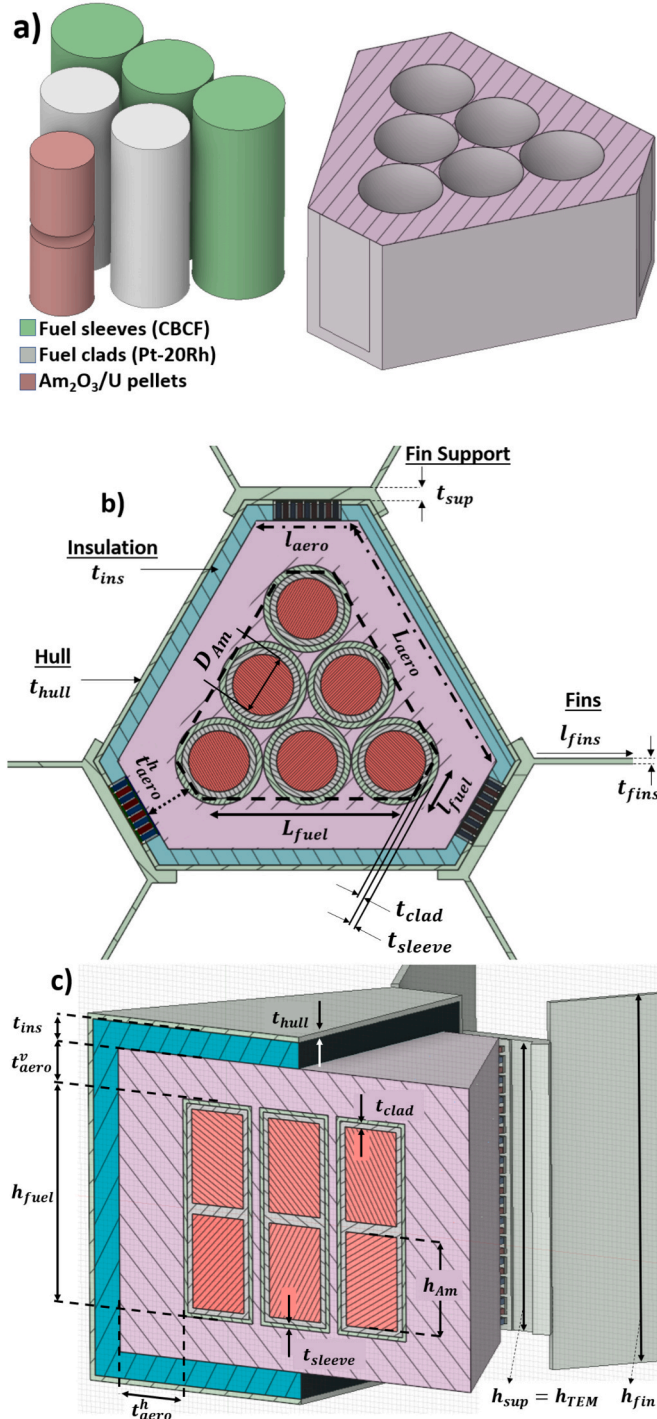
Fig. 1. A) assembly of the ELHS (european large heat source), b) top-view and c) front-view section of the RTG components and respective design parameters, along with a depiction of the pseudo-volume used in the network model (dashed lines in b). in 1a, CBCF stands for carbon-based carbon fibers, the material used for the sleeves.

three simple parameters, the dimensions of a) the short side, $l_{\text{fuel}} = 0.5 \bullet (D_{\text{Am}} + 2 \bullet t_{\text{clad}} + 2 \bullet t_{\text{sleeve}})$, b) the long-side, $L_{\text{fuel}} = 2.5 \bullet (D_{\text{Am}} + 2 \bullet t_{\text{clad}} + 2 \bullet t_{\text{sleeve}})$, and c) the height of the pseudo-volume, $h_{\text{fuel}} = 2 \bullet h_{\text{Am}} + 4 \bullet t_{\text{clad}} + 2 \bullet t_{\text{sleeve}}$, considering each Am-pellet to be enclosed in its own clad. Fig. S3 in the ESI (Electronic Supplementary Information) described the methodology followed to derive the dimensions of the sides of the truncated triangle. This pseudo-volume is extremely useful as the dimensions of all outer RTG

components can be expressed in relation to it. For example, as depicted in Fig. 1b for the aeroshell, the dimensions of a) its short-edge will be equal to $l_{\text{aero}} = l_{\text{fuel}} + \sqrt{4/3} \bullet t_{\text{aero}}^h$, b) its long-edge will be equal to $L_{\text{aero}} = L_{\text{fuel}} + \sqrt{4/3} \bullet t_{\text{aero}}^h$, and c) its height will be equal to $h_{\text{aero}} = h_{\text{fuel}} + 2 \bullet t_{\text{aero}}^v$. Here, t_{aero}^h and t_{aero}^v are the horizontal thickness of the aeroshell (i.e. in the direction of the heat flow) and the vertical thickness, respectively. For simplification, we assume t_{aero}^h and t_{aero}^v to be constant across all sides. With these approaches in mind, and for the aeroshell outer dimensions to be equal to the ELHS, the set of dimensions selected were $t_{\text{clad}} = 2$ mm, $t_{\text{sleeve}} = 1.5$ mm, $t_{\text{aero}}^h = 27.7$ mm and $t_{\text{aero}}^v = 16$ mm. Because of the restrictions related to mesh generation, which are discussed in Section 4 of the ESI, the sleeves were moved slightly outwards in the 3D FEA, leading to t_{aero}^h being 25 mm instead of 27 mm, however the volumes of all ELHS components remained identical between the two models.

Regarding the outer RTG components beyond the inner core, TEMs are placed on the short-side edges, with their hot junction in contact with the aeroshell and their cold junction in contact with a structural support with two radiative fins per TEM mounted on it. On the lateral sides of the TEM and on the long-side edges of the aeroshell, as well as on the base and top areas of the aeroshell in case of a single RTG unit, a thermal insulation layer is placed. Outside this insulation layer, a metallic casing, referred to as the hull, is used to contain the RTG assembly. In the NM, the insulation (l_{ins}, L_{ins} and h_{ins}) and hull (l_{hull}, L_{hull} and h_{hull}) can be expressed in relation to the outer aeroshell surfaces using thickness parameters, t_{ins} for the insulation layer and t_{hull} for the hull, following the same relationship as l_{aero}, L_{aero}, and h_{aero}, respectively. These thicknesses are considered constant both at the short and long sides as well as at the top/bottom of the RTG. Similarly, the support thickness is denoted as t_{sup}, while l_{fin} and t_{fin} are the length and the thickness of the fins, respectively. The height of the fins, h_{fin}, is considered equal to the total RTG height, spanning the edges of the hull, i.e. equal to h_{hull}, while for a scaled-up RTG with several stacked ELHS it should be taken equal to the height of the ELHS. These dimensions, along with the components they represent, are shown in Fig. 1b and c and are also collectively described in the nomenclature Table in the ESI.

Regarding the TEMs, depicted in Fig. 2a and b, h_{TEM} and w_{TEM} are the height and the width of the TE module while t_{housing} is the total thickness of the housing that encloses the TE legs. The housing is composed of ceramic layers and copper bridges and is calculated as $t_{\text{housing}} = 2(t_{\text{ceram}} + t_{\text{Cu}})$, where the "2" accounts for the ceramic plates and copper bridges being distributed equally in both the hot and the cold junctions. Consequently, the leg length can be calculated from $l_{\text{TE leg}} = t_{\text{ins}} + t_{\text{hull}} - t_{\text{housing}}$. The parameter l_{gap} is the gap width in between neighboring legs, thus determining the fill factor which is the ratio of the total area of the TE legs related to the area of the ceramic plate in contact with the aeroshell. As described later, the width of the p- and n-type legs, w_p and w_n, respectively, is determined from the cross-section area ratio of the TE legs through the calculation of the optimum current which maximizes the power output. To reduce the number of variables, both leg types are considered as square-shaped and the minimum width for the thinner TE leg is set to 2 mm. To determine the number of pn-couples for given w_p and w_n, the model executes three steps, depicted graphically in Fig. 2c: initially (step 1), it will maximize the integer number of couples placed along the short TEM edge, i.e. along w_{TEM}, keeping a distance of l_{gap} between subsequent legs and half this distance between the leg and the edges of the module. Subsequently (step 2), the model will check whether there is sufficient space to place an additional row of pn couples rotated along the long TEM edge (h_{TEM}) (step 2). Finally (step 3), the model will fill the remaining module area with the maximum number of pn couples, keeping the same couple placements determined from steps 1 and 2 and maintaining a distance of l_{gap}.

In their RTGs, NASA filled the gaps in-between neighboring TE legs with thermal insulation [40,54,55]. This insulation, beyond acting as a
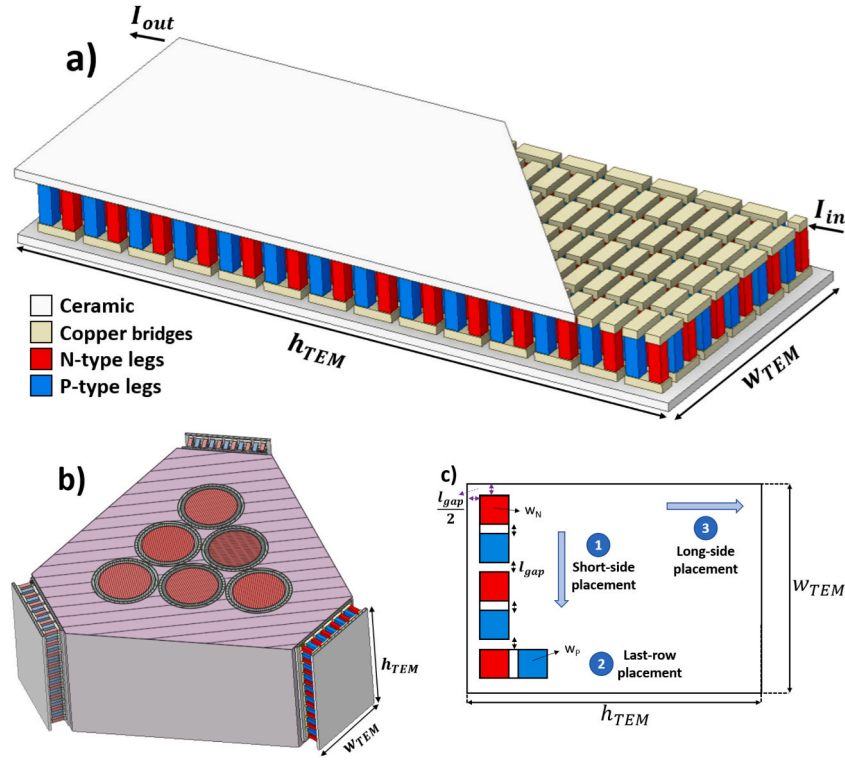
Fig. 2. A) TEM components along with the input and output current on the copper bridges used in the fea model, b) placement of the TEM on the aeroshell short-edge and c) steps to fill the TEM with pn-couples in the nm.

mechanical support, prevents thermal radiation loss between the open surfaces of the module, a phenomenon that can considerably reduce module efficiency, particularly at elevated hot-side temperatures typical of SiGe-based RTGs. Simultaneously, however, thermal insulation also creates an additional thermal bypass within the TEM by conduction, but Li *et al.* [54] identified that in their high-temperature SiGe module, this effect is much weaker compared to a thermal bypass by radiation. As radiative heat transfer is approximately $\propto T^3$ and we are looking only at relatively low TEM hot side temperatures we have neglected radiative heat transfer through the TEM in this study.

2.2. Material properties and limitations

Most of the materials selected for the RTG components here are taken from Ambrosi *et al.* [12]. However, when material data were not available in [12], data from other sources was used. As all components except the TEM are modelled here as passive thermal resistors and the focus is on steady-state calculations, the required properties relevant for the employed materials are the thermal conductivity and the mass density to estimate the components (and thus the system's) mass. The properties used for the RTG components as well as their references are presented in Table 1. Detailed discussion and reasoning on material selection is presented in Section 1 of the provided ESI. While the thermal conductivity of each material in Table 1 is taken as temperature-independent, the chosen value corresponds to the temperature range each component is expected to reach during operation. Details about the expected operating temperature of each component is also presented in the ESI. In addition, CBCF in Table 1 corresponds to Carbon-Based Carbon Fibers, the material considered for the sleeves while Am$_2$O$_3$-U stands for (Am$_{0.8}$U$_{0.12}$Np$_{0.06}$Pu$_{0.02}$)O$_{1.8}$, the chemical composition of the uranium-stabilized Am$_2$O$_3$ used in the ESA RTG and developed by Vigier *et al.* [56].

For the TE material in the ESA RTG, a selenium- and antimony-alloyed bismuth telluride module was employed, however the precise composition was not disclosed [12]. Consequently, we chose data from

Table 1
Material properties used for the RTG components. The magnitude of the thermal conductivity corresponds approximately to the temperature each material is expected to have during operation, with detailed discussion presented in the ESI.

Material	Component	Density [kg/m³]	Thermal Cond. [W/(mK)]	Ref.
Am$_2$O$_3$-U	Fuel pellets	$1.07 \cdot 10^4$	1.2	[56,57]
Pt-Rh	Clad	$1.87 \cdot 10^4$	49.2	[58]
CBCF	Sleeves	$1.8 \cdot 10^2$	0.25	[59]
SEPCARB	Aeroshell	$1.75 \cdot 10^3$	50	[60]
KDYS-4Aerogel	Insulation	$2.5 \cdot 10^2$	0.018	[49]
AM162	Hull/Fins	$2.1 \cdot 10^3$	210	[61]
Copper	TEM bridges	$8.96 \cdot 10^3$	400	[62]
Al$_2$O$_3$	Ceramichousing	$3.72 \cdot 10^3$	24.7	Measuredin-house

Zhu *et al.* [63] as they not only report material properties but also module data, indicating some maturity of the TEM. Specifically, a combination of *n*-type Bi$_{1.8}$Sb$_{0.2}$Te$_{2.7}$Se$_{0.3}$ + 15 wt% Te and *p*-type Bi$_{0.5}$Sb$_{1.5}$Te$_3$ TE legs are considered, for which Zhu *et al.* [63] reported a 6.6 % conversion efficiency. The temperature-dependent TE properties are shown in Fig. S1 of the ESI. The material density we considered for the *n*- and *p*-type legs is $6.88 \cdot 10^3$ kg/m^3 [64] and $7.28 \cdot 10^3$ kg/m^3 [63], respectively. The temperature-dependent electrical resistivity of the copper bridges is shown in Fig. S2 of the ESI.

Bi$_2$Te$_3$-based alloys are a benchmark TE material because of their impressive TE properties around room temperature, however they are limited to low operating temperatures of up to around 523 K, beyond which they undergo decomposition [49]. In addition, for the Pt-20 % Rh cladding, Ambrosi *et al.* highlight the formation of an intermetallic at 1473 K, which, when formed, will degrade the properties of the cladding [12]. In the presence of americium, both Rh and Pt form intermetallics; specifically, Rh$_3$Am forms at 1823 K, Pt$_2$Am forms at 1673 K and Pt$_5$Am forms at 1473 K [65]. Moreover, Pt and Rh form eutectics with C at

temperatures around 1973 K [66,67], a potentially relevant reaction as the cladding is in contact with the carbon-based sleeve. In addition, as reported by Inouye *et al.* [68], Pt-Rh-based alloys are resistant to oxidation at temperature up to 1473 K, with minor weight changes as a result of oxide formation. Consequently, adopting the 1473 K temperature limit for the cladding is a reasonable assumption to prevent degradation of the Pt-Rh properties. In our study, both these upper temperature limits are considered during design optimization. On the outer RTG surfaces, i.e., hull and fins, application of a coating layer is a well-known method to increase emissivity [69]. In fact, the MMRTG employs a white coating material with a high emissivity, which is effective at both reflecting solar radiation as well as increasing the radiative heat emitted from the fins [37]. The ESA RTG presumably utilizes a similar coating as well [38], however no specific values were reported. Here, as we neglect exposure to solar radiation, we assume grey body emissivity. The spectral emissivity of the outer hull surfaces, consisting of a 62 % aluminum-38 % beryllium alloy, was set equal to 0.4, determined from the emissivity of their pure metallic forms [70] and the volumetric composition of the alloy, while for the fins we assumed an emissivity of 0.95 [71].

2.3. Thermoelectric network model

2.3.1. Modeling the RTG components

The heat emitted by the fuel pellets, $\dot{Q}_{\text{fuel}}$, can be considered to take two paths only. On the first path, referred to as the TEM branch, after passing through the aeroshell, a fraction of the heat flow, $\dot{Q}_{\text{TEM-In}}$, enters the TEM. This heat will create the temperature difference along the TE legs, and a portion of $\dot{Q}_{\text{TEM-In}}$ will be converted into electrical power output. The remaining heat, $\dot{Q}_{\text{TEM-Out}}$, travels from the TEM's cold side through the support into the fins where it will be radiated to the environment. In the second path, referred to as the thermal bypass branch, $\dot{Q}_{\text{By}}$, the remaining portion of $\dot{Q}_{\text{fuel}}$ is transmitted through the insulation layer to the hull where it will be radiated to the environment. For all calculations of this branch, both the side surfaces as well as the top and bottom surfaces of the RTG are considered as we investigate a single RTG unit configuration. Thus, even though the NM does not consider out of plane heat fluxes explicitly, the relevant contribution of the top and bottom surfaces to radiative exchange with the environment is taken into account. Based on these principles, the TE NM of the RTG is sketched as an analogue circuit, with each path including a series of

elements that represent the RTG components, schematically drawn in Fig. 3. The temperature of the environment, referred to as T_{env} has been set to 220 K, which corresponds to the average temperature around the polar areas of the Moon [72].

Among the elements of the model in Fig. 3, most of them represent thermal resistances that are purely conductive. These include the clad, sleeves, aeroshell, insulation, hull and support. Thermal interface resistances between neighboring components have a detrimental effect on the temperature profiles and power output of the overall system [73]. Practically these can be minimized constructively, e.g. by high surface quality or by applying mechanical pressure and/or thermal grease in the contact regions [74,75]. As the magnitude of the thermal interface resistances is not reported [12], they are neglected in the current study, but can be implemented in a straightforward manner by adding further resistive elements to the NM.

For clad, sleeve, aeroshell, insulation, hull and support components, effective and temperature-independent material properties are considered, leading to an approximately linear temperature profile. For purely conductive elements with no thermal contact resistance, the temperature profile can be calculated using the integrated form of Fourier's formula, as per Eq. (1).

$$\dot{Q}_{\text{Fourier}} = \frac{\Delta T}{W_i} \tag{1}$$

$$W_i = \frac{t_i}{\kappa_i \bullet A_{\text{eff}}} \tag{2}$$

Here, W_i is the thermal resistance of the element in question and it is calculated using t_i and A_{eff}, i.e. the thickness and effective cross-section area of the element in the path of the heat flow, respectively. Given the truncated-triangle shape of the RTG, the cross-section area of each element changes from its inner to its outer surface so for simplification A_{eff} is considered as the average of these two surfaces.

In the TEM branch, the supports are considered as conductive elements with a non-negligible thermal resistance, but radiative heat transfer from them is neglected based on the much larger area of the fins to simplify the model. Within the support volume, the heat flow is redirected perpendicularly towards the fins. Consequently, as depicted graphically in Fig. 4, $\dot{Q}_{\text{TEM-Out}}$ is divided into two equal fractions each traveling towards one of the fins, thus Eqs. (1) and (2) are solved considering the support's perpendicular length, l_{sup}, i.e. the distance between the support's central point and the base of the fins, while $A_{\text{eff}} =$
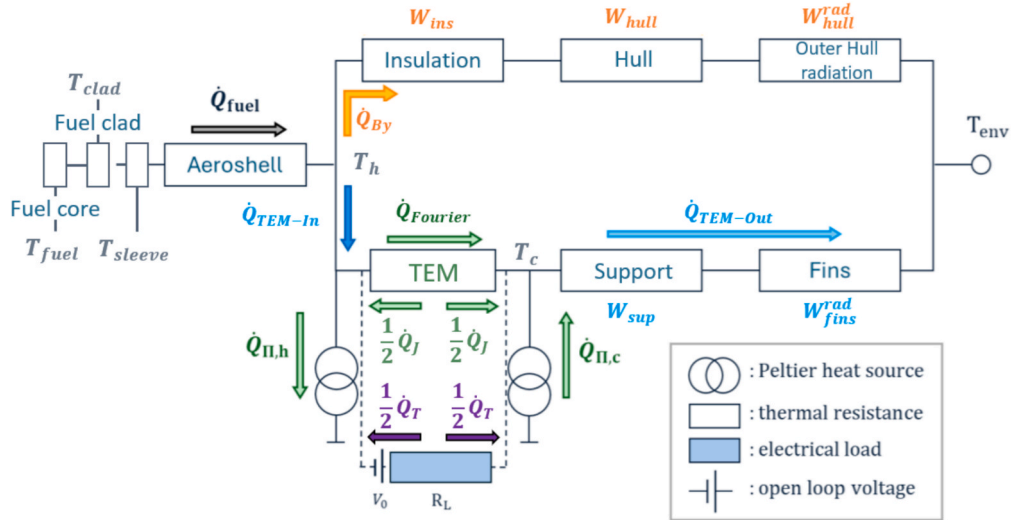

Fig. 3. Schematic of the thermoelectric network model, showcasing the RTG components that constitute it, as well as the heat flows considered. Note that the sketched Thomson heat flow, $\dot{Q}_{\text{T}}$, and Joule heat flow, $\dot{Q}_{\text{J}}$, to the hot and cold side hold only approximately, but are considered correctly in the actual calculations. Thermal connections between components are represented by solid lines, while the electrical circuit is depicted by dashed lines.
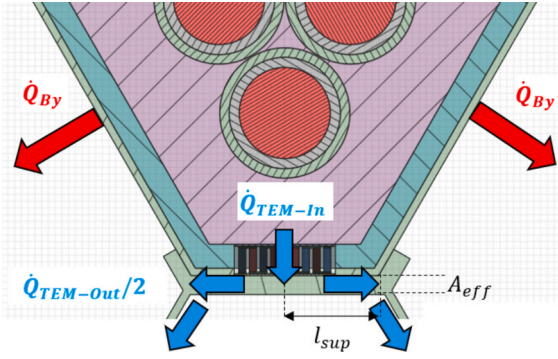
Fig. 4. Schematic of the heat flowing through the TEM and outwards towards the environment, as well as of the heat moving through the bypass branch. Along the support, the heat moving out of the TEM, $\dot{Q}_{\text{TEM−Out}}$, is split equally and traverses perpendicularly towards the two fins, where it is radiated to the environment.

$t_{\text{sup}} \bullet h_{\text{sup}}$, with t_{sup} being the support's thickness and h_{sup} its height. In the network model, l_{sup} and h_{sup} are dependent on the dimensions of neighboring RTG components, i.e. equal to half the length of the outer short side of the hull, $l_{\text{hull}}/2$, and equal to the height of the TEM, h_{TEM}, respectively. This coupling simplifies the support optimization to a single parameter, i.e. its thickness.

The outer hull surface and the fins radiate the heat passing through them to the environment. For the outer hull surface, the heat exchanged can be calculated using the Stefan-Boltzmann law, shown in Eq. (3).

$$\dot{Q}_{\text{By}} = \varepsilon \sigma A_{\text{hull}} \left(T_{\text{c,hull}}^4 - T_{\text{env}}^4 \right) \tag{3}$$

Here, ε is the emissivity, σ is the Stefan-Boltzmann constant, A_{hull} is the outer surface area of the hull and $T_{\text{c,hull}}$ is the outer surface temperature. To calculate the inner hull temperature, $T_{\text{h,hull}}$, Eq. (1) would then be solved. For the fins, however, conduction and radiation are coupled along their length, thus the consideration of a linear temperature profile would be incorrect. For this reason, a unidirectional discretization of the fins into 50 slices along the fin length, l_{fin}, is used to solve the heat balance equation and thus obtain a precise temperature profile using Eq. (4).

$$\frac{d^2 T(x)}{dx^2} = \frac{\Pi_{\text{fin}} \varepsilon \sigma}{A_{\text{fin}} \bullet \kappa_{\text{fin}}} \left(T(x)^4 - T_{\text{env}}^4 \right) \tag{4}$$

In this equation, $T(x)$ is the temperature along the fin length, $\Pi_{\text{fin}} = 2 \bullet \left(t_{\text{fin}} + h_{\text{fin}} \right)$ is the perimeter of the slice determined using the thickness, t_{fin}, and the height, h_{fin}, of the fins (the latter is set equal to the height of the RTG's outer hull as a single RTG unit is investigated) and $A_{\text{fin}} = t_{\text{fin}} \bullet h_{\text{fin}}$ is the cross-section area of each slice along the fin length. This ordinary differential equation is solved for the following boundary conditions: For the base of the fin, the heat flow is set to $\dot{Q}_{\text{TEM−Out}}/2$ and only conduction is considered, i.e. $\frac{dT_{\text{fin−h}}}{dx}\Big|_{(x=0)} = -\frac{\dot{Q}_{\text{TEM−Out}}/2}{\kappa_{\text{fin}} \bullet A_{\text{fin}}}$, allowing the calculation of the fin root temperature, $T_{\text{fin−h}}$. At the outer edge of the fin, no heat conduction occurs so only radiative losses to the environment are taken into account, i.e. $\frac{dT_{\text{fin−c}}}{dx}\Big|_{(x=L)} = 0$, with $T_{\text{fin−c}}$ being the fin temperature at the edge. A sketch showcasing the temperature profile calculation along the fin length is presented in Fig. S4 of the ESI.

Ambrosi *et al.* [12] mention that the critical temperature that the Am$_2$O$_3$ pellets should not exceed is 1973 K. Although the current RTG design with the Bi$_2$Te$_3$ as its TE module is unlikely to reach such temperatures, it is important to track the temperature of the fuel core when higher operating temperature TE materials are utilized. Within the fuel pellet, conduction and heat generation are coupled using the general heat balance equation for a heat generating cylinder, Eq. (5), which can

be solved to derive the temperature profile, Eq. (6), using a set of boundary conditions.

$$\frac{\partial^2 T_{\text{Am2O3}}(r)}{\partial r^2} + \frac{1}{r} \frac{\partial T(r)}{\partial r} = -\frac{\alpha_{GF} \bullet q_{\text{gen}}}{\kappa_{\text{Am2O3}}} \tag{5}$$

$$T_{\text{Am2O3}}(r) = T_{\text{Am2O3−c}} + \frac{\alpha_{GF} \bullet q_{\text{gen}}}{2\kappa_{\text{Am2O3}}} \left(R_{\text{pel}}^2 - r^2 \right) \tag{6}$$

Here, $T_{\text{Am2O3−c}}$ is the temperature at the outer surface of the pellet (adjacent to the clad), R_{pel} is the radius of the cylindrical pellet and q_{gen} is the volumetric heat generation rate from radioactive decay. The boundary conditions considered are a) $T_{\text{Am2O3}} \left(r = R_{\text{pel}} \right) = T_{\text{Am2O3−c}}$ at the edge of the cylinder, with $T_{\text{Am2O3−c}}$ being equal to the hot side temperature of the clad, and b) $\frac{\partial T}{\partial r}\Big|_{(r=0)} = 0$, i.e. the temperature at the core of the fuel pellet. With our approach, we neglect the heat lost on the base and top of the americium pellet, as that would require the solution of a 2D partial differential equation. However, as an approximation, to take into account that only a portion of the total heat would pass through the side surface, we introduced the geometrical factor $\alpha_{GF} = \frac{2\pi R_{\text{pel}} \bullet h_{\text{Am}}}{2\pi R_{\text{pel}} \left(h_{\text{Am}} + R_{\text{pel}} \right)}$, which is the ratio of the side cylindrical surface to the total surface of the cylindrical pellet and corresponds to ~72 %.

An important assumption made in the network model to simplify the calculations is that the two branches, "TEM" and "Bypass", are thermally independent, which means that they don't exchange heat with each other. In other words, NM elements of the two branches that are in direct vicinity in reality, e.g. contacts between TEM housing with insulation and with hull as well as between hull and support, are assumed to be perfectly insulated and no heat transfer is allowed, which might be achieved practically to a very good extent by the use of thin, thermally insulating layers between the components. We have run simulations with and without heat exchange in all of these contact regions, which resulted in temperature and power output deviations around 0.6 % and 1.6 %, respectively, justifying this simplification. Detailed comparison of the results will be presented in Section 3.2.

2.3.2. Thermoelectric performance calculation

Solving the network model to calculate the temperatures, heat flows and performance of the RTG is an iterative process, with the overall workflow presented schematically in Fig. 5. As a starting condition, the heat produced by the fuel is equally distributed in the two branches, i.e. $\dot{Q}_{\text{TEM−In}} = \dot{Q}_{\text{By}} = \dot{Q}_{\text{fuel}}/2$ (step 1 in Fig. 5). Subsequently, moving from the environmental temperature towards the RTG core and calculating the outer surface radiation, i.e. Eq. (3) for hull and Eq. (4) for fins, and inner component conduction, i.e. Eq. (1), the model calculates the inner and outer surface temperature of each component, T_i. This means that $\dot{Q}_{\text{By}}$ will determine the temperature at the outer surface of the aeroshell, which is assumed equal to the hot-side temperature of the TEM, T_h, while $\dot{Q}_{\text{TEM−Out}}$ (assumed equal to $\dot{Q}_{\text{TEM−In}}$ for the first iteration) will determine the cold-side temperature of the TEM, T_c, completing step 2 of Fig. 5.

From this point onwards, calculations transition from the system level, i.e. from $\dot{Q}_{\text{TEM−In}}$ flowing through the RTG components, to the TE leg level with area-specific terms such as the heat flux, $q_{in,m}$, the power density, $p_{j,m}$, and the current density, $j_{opt,m}$, of the "m"-type leg. The subscript "m" refers to the type of the TE leg, i.e. p or n-type. In addition, all TE-related properties, i.e. thermal and electrical conductivity and Seebeck coefficient, are now considered temperature-dependent, expressed through 3rd-order polynomial functions and derived from the experimental characterization of the utilized TEM (Fig. S1 of the ESI). In case material properties beyond the experimentally-determined temperature range are needed, these will be extrapolated.

The TEM's ceramic layers and contact resistances cause a reduced temperatures difference at the TE material, $\Delta T'_{\text{TEM}} = T_{h'} - T_{c'}$, compared
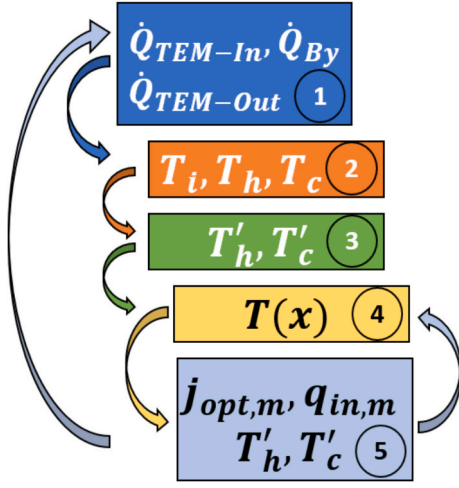
Fig. 5. Flowchart representing the iterative solution process of the network model. The heat flows through the RTG components, $\dot{Q}_{TEM-In}$, $\dot{Q}_{TEM-Out}$ and $\dot{Q}_{By}$, determine the temperature profiles of the components (T_i) as well as the hot and cold side temperature of the TEM (step 2). Step 3 then calculates the temperatures at the hot and cold side of the TE legs, T'_h and T'_c, which act as the base for the calculation of the temperature profile within the leg, T(x), (step 4), and of the current density, $j_{opt,m}$, and heat flux, q_{in}, (step 5), for each "m"-type leg. The numbered circles showcase calculation steps and the arrows represent the iterative process.

to the outer temperatures at the TEM, $\Delta T_{TEM} = T_h - T_c$:

$$T'_i = T_i \mp \frac{(T_h - T_c)}{2} \bullet (1 - \nu_{therm}) \qquad (7)$$

Eq. (7) considers this by introducing a correction term, $\nu_{therm} = \frac{1}{1+2\bullet f_{pel}\frac{w_c}{w_{TE}}}$, whose magnitude depends on the relation between Fourier and Peltier heat and is in general different for *p*- and *n*-type legs, therefore it is written here leg-specific in intensive quantities instead of extensive quantities. w_{TE} is the average area-specific thermal resistance of the TE leg, obtained by temperature averaging of the thermal conductivity, κ_m, i.e. $w_{TE} = \frac{l_{TE\,leg}}{\Delta T} \int (\kappa_m)^{-1} dT$. The calculation of the Peltier factor, $f_{pel} = 1 + zT_m/2$, uses the temperature averaged figure of merit, zT_m. The term $w_c = t_{housing}/(2 \bullet k_{Al2O3}) + w_{interf}$ represents the thermal resistivity of the ceramic housing, with w_{interf} being the area-specific interface thermal resistivity, assumed to be zero here. The calculation of T'_h and T'_c from Eq. (7) completes step 3 of Fig. 5.

For an accurate estimation of the energy flows, material properties and temperature distribution inside the TEM, the temperature profile along the leg needs to be calculated using the thermoelectric heat balance equation [73,76]:

$$\kappa_m \frac{\partial^2 T}{\partial x^2} + \frac{\partial \kappa_m}{\partial T} \left(\frac{\partial T}{\partial x}\right)^2 - j_{opt,m} \bullet T \frac{\partial \alpha_m}{\partial T} \frac{\partial T}{\partial x} = -j_{opt,m}^2 \bullet r_m \qquad (8)$$

Eq. (8) considers terms for Fourier, Thomson and Joule heat contributions along the TE leg itself and it is solved through an iterative process. The iterations are terminated when the root mean square difference of two subsequent T(x) profiles drops below a certain convergence limit, ΔT_{conv}. The term $j_{opt,m}$ refers to the optimal current density for maximum power output, calculated from Eq. (9).

$$j_{opt,m} = \frac{\int_{T'_c}^{T'_h} \alpha_m(T) dT}{2(r_m + 2r_c)} \qquad (9)$$

Here $\alpha_m(T)$ is the Seebeck coefficient and r_m is the area-specific electrical resistivity of the "m"-type leg, while r_c is the area-specific electrical contact resistance, assumed equal to zero here. While $\alpha_m(T)$ is calculated through temperature integration, r_m is obtained by spatial

averaging using the employed temperature profile, i.e. $r_m = \int_0^{l_{TE\,leg}} \rho_m(T(x)) dx$, with ρ_m being the electrical resistivity of the TE material. With the obtained temperature profile and current density, the heat flux at the hot side of the leg can be calculated from Eq. (10):

$$q_{in,m} = \kappa_m(T'_h)\frac{dT}{dx}\bigg|_{x=0} + \left(1 - \frac{w_{interf}}{w_m}\right)j_{opt,m} \bullet \alpha_m(T'_h) \bullet T'_h - r_c\frac{j^2_{opt,m}}{2} \qquad (10)$$

Where $x = 0$ corresponds to the hot side of the TE leg. The third term considers additional Joule heat from the electrical contact resistances while the second accounts for the distribution of the generated Peltier heat depending on the ratio of thermal interface resistance and leg thermal resistance.

With the calculation of $q_{in,m}$ within the iterative loop, the inner temperatures of the TE leg, T'_h and T'_c can now be updated from $T'_h = T_h - q_{in,m} \bullet w_c$ and $T'_c = T_c + q_{out,m} \bullet w_c$, respectively, which allows for more accurate predictions compared to Eq. (7) thus replacing the values calculated from step 3. $q_{out,m}$ is calculated using Eq. (10) at the cold side of the TE leg. However, as new T'_h and T'_c are calculated, they are fed back into step 4 of Fig. 5 to re-calculate $T(x)$ from Eq. (8), $j_{opt,m}$ from Eq. (9) and $q_{in,m}$ from Eq. (10) through an iterative loop. This loop converges when a convergence criterion, Δj_{conv}, is reached, which is determined by the changes of $j_{opt,m}$ between subsequent iterations. In each step of this iterative process, the material properties, α_m, r_m and κ_m, are constantly updated based on the new temperature profile.

After the convergence of the temperature profile and $j_{opt,m}$, the generated power density, $p_{j,m}$, of the "m"-type leg can be calculated from Eq. (11), thus completing step 5 of Fig. 5.

$$p_{j,m} = j_{opt,m}\left(\int_{T'_c}^{T'_h} \alpha_m(T) dT - j_{opt,m} \bullet r_m\right) \qquad (11)$$

The calculated $j_{opt,m}$ for the *p*- and *n*-type legs is then used to define the area ratio of the TE legs, given by $\frac{A_p}{A_n} = \frac{j_{opt,n}}{j_{opt,p}}$, accounting for the fact that all legs are connected electrically in series and hence the current is fixed to a unique value for both leg types. The calculated $q_{in,m}$ and $p_{j,m}$ for the *p*- and *n*-type TE legs are multiplied by the respective cross-section area of the legs and multiplied by the total number of thermocouples, n_{pairs}, to return to the system level and estimate the total heat flow in the TEMs, $\dot{Q}_{TEM-In}$, and the total power production of the RTG, P_{TEM}, for current $I_{opt} = j_{opt,n} \bullet A_n = j_{opt,p} \bullet A_p$, as per Eq. (12) and (13), respectively.

$$\dot{Q}_{TEM-In} = \left(q_{in,n} \bullet A_n + q_{in,p} \bullet A_p\right) \bullet n_{pairs} \qquad (12)$$

$$P_{TEM} = (p_{j,n} \bullet A_n + p_{j,p} \bullet A_p) \bullet n_{pairs} \qquad (13)$$

The calculated values of $\dot{Q}_{TEM-In}$ and P_{TEM} are fed back into step 1 of Fig. 5 and update $\dot{Q}_{TEM-Out} = \dot{Q}_{TEM-In} - P_{TEM}$ and $\dot{Q}_{By} = \dot{Q}_{fuel} - \dot{Q}_{TEM-In}$ in the RTG system level, completing the iteration and acting as the initial point of the subsequent iteration. This is the third and final iterative process, which lasts until the difference in $\dot{Q}_{TEM-In}$ between the current and previous iteration reaches a certain convergence criterion, $\Delta \dot{Q}_{conv}$. With the completion of the iterative steps the TE NM calculates the RTG state, i.e. temperature profiles, $\dot{Q}_{TEM-In}$, $\dot{Q}_{TEM-Out}$ and P_{TEM}, when it is operated at a current of $I_{opt} = j_{opt,n} \bullet A_n = j_{opt,p} \bullet A_p$. The operating voltage of the RTG, assuming connection in series for all involved TEMs, can be calculated from $V_{TEM} = P_{TEM}/I_{opt}$. The NM is also able to produce the P-I curve through the process described in Section 2.1 of the ESI, calculating the RTG state for every current in-between the open-circuit (OC) and short-circuit (SC) current magnitude.

2.4. Optimization using a genetic algorithm (GA)

The described NM is able to accommodate various dimensions for the

RTG components, calculate the temperature and heat flow within each component and predict the RTG's performance. As such, it forms the basis to perform a design optimization study using a Genetic Algorithm (GA) model [77]. During initialization, a large set of designs are created using randomly generated values within a specified range for each design parameter introduced in Sections 2.1 and 2.3. The parameters and corresponding ranges considered can be seen in Table 2.

Parameters not listed in Table 2 were not involved in the design optimization and are maintained constant or are interdependent. Regarding the former, the ELHS parameters, D_{Am}, h_{Am}, t_{aero}^h, t_{aero}^v, t_{clad} and t_{sleeve}, kept their original values described in Section 2.1 to ensure that in the optimized RTG geometry the safety protocols are adhered to. Moreover, the w_{TEM} and h_{TEM} are also kept constant. Generally, it is required for an efficient optimization that the number of variables is reduced as much as possible, in particular, the parameter space should not contain extraneous degrees of freedom. For the current RTG design, we have observed that the optimization process tends to maximize the cross-section area of the thermoelectric module. This is because larger modules will reduce the available area for insulation hence reducing the bypass losses. The observed dependence is weak and this simplification could break down if radiation losses through the module are introduced without any preventing measures; regardless, in the current version of the model, this phenomenon is neglected. Consequently, we decided to keep the module cross-section area fixed and maximized to begin with, allowing only a small gap of 2.5 mm around the modules for thermal insulation to be installed which will provide mechanical stability.

The generated designs, expressed by a list of the optimizable parameters, are simulated by the NM and are subsequently ranked based on a fitness coefficient which is defined by the objective of the optimization. In this case, the goal is to maximize the specific power of the RTG, i.e. P_{TEM}/m_{RTG}. The best design of each generation is maintained unmodified for the subsequent generation to prevent loss of performance and ensure that the GA always moves towards higher specific powers. The procedure of the GA is similar to what is described in Hamdia *et al.* [78] and is outlined, together with the meta parameter choice in the ESI. Besides the fitness coefficient, two additional key criteria are considered during the evaluation step to prevent unrealistic designs. These refer to the safe operating temperature of both the cladding (1473 K) and the Bi_2Te_3 TE material (523 K). If in a produced design these values are exceeded, its fitness coefficient is automatically set to zero.

2.5. Finite elements analysis (FEA) model

To validate the network model and ensure that the approach considered produces reliable results, a 3D FEA model is employed for comparison. The 3D geometry was produced with the tools provided by ANSYS Workbench 2023 R1 version, specifically SpaceClaim for the geometry generation and Mechanical for the mesh generation and TE calculations. The dimensions of the ELHS and the material properties of all RTG components are the same as those described in Sections 2.1 and 2.2. The remaining outer components, i.e. insulation, hull, TEM, support

Table 2
Parameters and value range considered for the design optimization study using the GA. Note that the TE leg length, $l_{TE\,leg}$, is coupled to the thickness of the housing. Design parameters not listed here will have a fixed value or they are dependent on other parameters.

Parameter	Minimum value [mm]	Maximum value [mm]
t_{ins}	5	25
t_{hull}	2	5
t_{sup}	2	8
L_{fin}	50	300
t_{fin}	2	5
$t_{housing}$	1	6
l_{gap}	1	5

and fins, are set to the dimensions of the optimized geometry calculated by the GA method described in Section 2.4.

Two FEA models are produced in this study. To achieve a direct comparison, the first 3D model replicates the same thermal and TE behavior as the NM by considering two independent heat transfer branches with no heat exchange between them. This means that in the FEA, heat transfer interfaces between the TEM and the insulation or hull components, as well as those in-between the hull and the support plates, are treated as perfect insulators. In the second 3D model, heat exchange is enabled between the two previously independent thermal branches. That means that perfect conduction, i.e. no interface resistance, is enabled in the contact regions between a) the TEM ceramic and the insulation at the hot side, b) the TEM ceramic and the hull at the cold side, and c) the support and the hull. To be able to control the interface heat exchanges in the two FEA cases, a non-conformal meshing strategy is used, which allows for more interface freedom compared to a conformal mesh, as in the latter specific interface control is not allowed. Details about the meshing approach are outlined in the ESI. To reduce the computational demands, the full 3D RTG volume was broken down into a 1/3rd axisymmetric geometry, allowing it to maintain the heat transfer symmetry present in the ESA RTG. A 1/3rd geometry is probably the smallest section that can be introduced, as slicing through the TEM would require the electric interconnections to be re-designed, which could introduce errors. As such, the final computational mesh consists of 0.67 M elements and 1.71 M nodes. A cut-view section of the 1/3rd axisymmetric RTG, as well as of the mesh details are shown in Fig. 6.

For the fuel pellets a volumetric heat generation on each pellet corresponding to a total thermal output of 200 W_{th}-axisymmetric equivalent of the whole system is defined. To define the electrical boundary conditions on the TEM, the outer connections of the terminating n- and p-type legs are set as ground and operating current, respectively. These connections can be seen as I_{in} (n-leg – ground) and I_{out} (p-leg – output) in Fig. 2a. Thermal radiation to the ambient environment was defined at the outer hull surfaces as well as on all faces of the fins, considering an environmental temperature of 220 K. Similar to
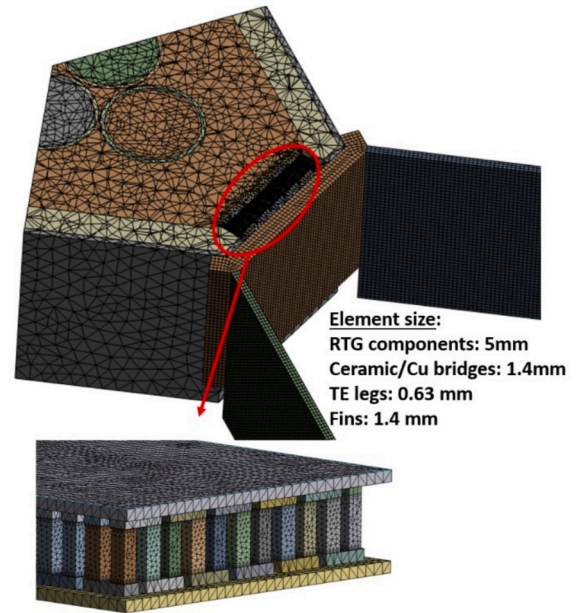
Fig. 6. A cut-view section of the axisymmetric RTG mesh and a close-up view of the TEM mesh used for FEA calculations. A non-conformal meshing strategy was used, and two cases were studied, one where conductive heat exchange between all connecting elements is enabled and one where heat exchange between the components of the TEM branch and the bypass branch is disabled, with the latter following the methodology of the NM.

the TE network model, the support is assumed to not radiate to the environment. At this stage, no surface-to-surface radiation is considered, which would account for radiative heat exchange between neighboring RTG surfaces based on a view factor, i.e. the relative exposure between the surfaces. Instead, outer surfaces are assumed to radiate fully to the environment. For the solution process, a steady-state simulation is considered, with convergence tolerance for heat flow, temperature, voltage and current of $0.5 \cdot 10^{-6}$ in the respective SI unit.

3. Results and discussion

3.1. Genetic algorithm optimization results

The evolution of the specific power associated with the best design of every generation can be studied to monitor the progress of the optimization and is displayed in Fig. 7, along with the respective power and mass values. The dimensions of the optimized RTG geometry as well as its performance, are presented in Table 3.

As seen in Fig. 7, the GA gradually improved the specific power, starting with an initial value of 1.14 W/kg which increased to a value of 1.36 W/kg after 30 iterations. Then, small gradual improvements led to the final value of 1.38 W/kg after 165 iterations. Past this point, the fitness parameter reaches a plateau and no further modifications happen, indicating that a global maximum has been reached. To better interpret the optimization results, the power and mass variations along the different generations are also displayed in Fig. 7. It is noteworthy that the power output underwent rapid oscillations in the first 50 iterations, until it reached a plateau with a maximum value of 14.67 W which corresponded to a specific power of 1.36 W/kg due to a relatively high system mass. Past this point, the GA made small incremental changes to both power and mass, continuously increasing the specific power by modifying the system component dimensions as seen in Fig. S5 of the ESI, until the maximum is identified. Here, to achieve the specific power of 1.38 W/kg, an electrical power output of 13.86 W and an RTG mass of 10.03 kg are estimated. This mass is distributed primarily along the ELHS components, which account for ~72 % of the total mass as can be seen in Fig. 8. The fins account for 13.4 % of the total mass, while the hull contributes by 4.5 %. The TEM accounts for 4.7 % of the total mass, with the ceramic and the copper bridges accounting for 31 % of the TEM mass each, while the *p* and the *n* type legs account for 21 % and 17 %, respectively. The remaining components account for around 2–3 % of
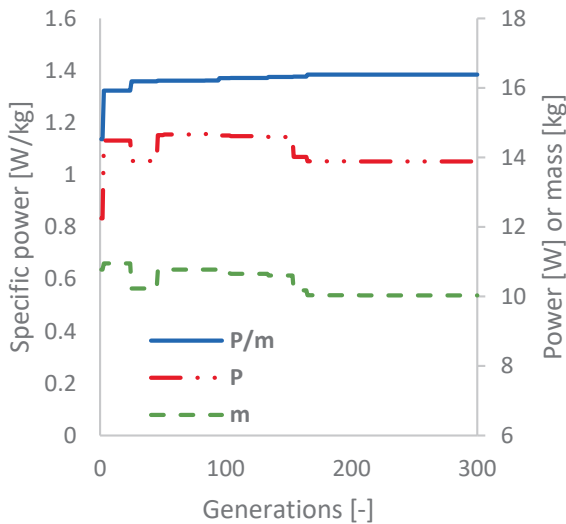
Table 3

Optimized RTG design parameters, as well as TE performance characteristics. "Fixed" refers to parameters whose value was kept constant during the GA optimization while "dependent" refers to parameters whose final value depends on their coupled parameters.

Parameter	Value	Unit
RTG design		
D_{Am} (fixed)	27	mm
h_{Am} (fixed)	35	mm
t_{clad} (fixed)	2	mm
t_{sleeve} (fixed)	1.5	mm
t_{aero}^{h} (fixed)	27.7	mm
t_{aero}^{v} (fixed)	16	mm
l_{aero} (fixed)	49	mm
L_{aero} (fixed)	117	mm
h_{aero} (fixed)	113	mm
t_{ins}	9.8	mm
t_{hull}	2	mm
t_{sup}	6.5	mm
l_{sup} (dependent)	31.3	mm
h_{sup} (dependent)	108	mm
L_{fin}	279.7	mm
t_{fin}	2.8	mm
h_{fin} (dependent)	136.6	mm
TEM design		
w_{TEM} (fixed)	44	mm
h_{TEM} (fixed)	108	mm
$t_{housing}$	5.5	mm
l_{gap}	1.6	mm
$l_{TE\ leg}$ (dependent)	6.3	mm
Area *p*-leg	4.59	mm^2
Area *n*-leg	4.0	mm^2
Total number of *pn* pairs	462	–
RTG performance		
Electrical power output	13.86	W
Opt. current	0.66	A
Mass	10.03	kg
Specific power	1.38	W/kg
Voltage	20.94	V
Energy conversion efficiency	6.9 %	–
$\dot{Q}_{TEM-In}/\dot{Q}_{fuel}$	85.5 %	–
T_h	522.1	K
T_{clad}	548.3	K

Fig. 7. Evolution of the highest specific power, P/m, and the corresponding electrical power output, P, and mass, m, of the RTG for each generation produced by the GA. The GA gradually improved the specific power over 300 generations, reaching a plateau after 165 iterations.
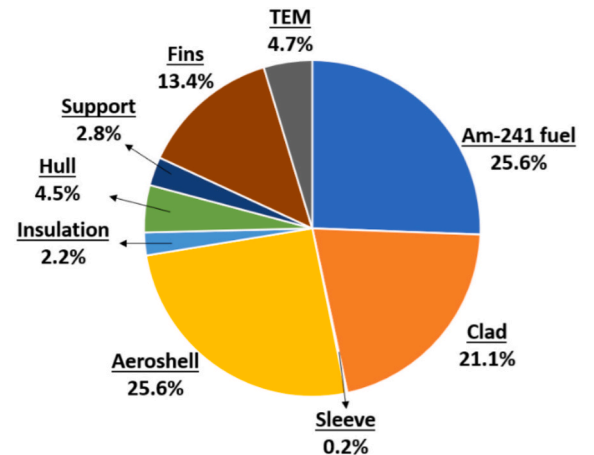

Fig. 8. Mass distribution of the optimized RTG components. The ELHS components, i.e., ^{241}Am, clad, sleeve and aeroshell, account for ~72 % of the total RTG mass and their dimensions were kept fixed in this study to ensure the safety protocols are adhered to.

the total mass each. Interestingly, our calculations estimate a mass of 7.26 kg for the ELHS, while Mesalam *et al.* reported a mass of 6.85 kg [24]. Even though our americium fuel pellets and aeroshell have the same dimensions as those of the ESA RTG [12], this is a reasonable deviation as data for the materials' density, as well as the exact thicknesses of the clads and sleeves, have not been reported.

To understand the influence of each design parameter on the RTG state, we need to examine them individually by changing their values within the permitted range while keeping all other design parameters in their optimized value, i.e. those presented in Table 3. However, the operating current was re-optimized with the parameter change to ensure that the RTG always operates at its maximum power. In several cases, the operating temperature exceeded the 523 K limit at the TEM hot-junction. For these cases, the TE properties were extrapolated using 3rd order polynomial equations. Examining only the influence of a single parameters is not always possible as some are interlinked. For example, changing the insulation thickness while keeping the housing and hull thicknesses constant will also change the TE leg length, so the observed influence will be a combination of both parameters. Since the TE leg length is far more influential than the housing thickness both in terms of temperature profiles and TE performance, we decided to keep the former fixed and equal to 6.3 mm, i.e. equal to the leg length of the optimized geometry. Consequently, the housing thickness will change accordingly to the insulation thickness to always keep the TE leg length fixed but also to keep the TEM physically connected to both ELHS and fin

Fig. 9. Impact of insulation thickness on a) specific power, power output and mass of the RTG and b) temperature on the hot and cold junction as well as on the relative heat flow in the TEM. The shaded region represents the insulation thickness where the safe operating temperature limit of the Bi$_2$Te$_3$ TEM, i.e. 523 K, is exceeded.

support. This influence is seen in Fig. 9, where t_{ins} changes from 6.5 to 12 mm while the housing thickness changes from 2.2 to 7.7 mm, respectively. The shaded region in Fig. 9 represents the insulation thickness where the maximum temperature for the safe operation of the Bi$_2$Te$_3$ TEM, i.e. 523 K, is exceeded.

Increasing the insulation thickness from 6.5 mm to 12 mm increases the specific power and power output by 0.03 W/kg and 1.15 W, respectively, while the mass of the RTG increases by only 0.64 kg. There are three factors that contribute to the mass increase. Firstly, thicker insulation translates to a volume, and hence a mass increase. Secondly, to keep a contact between the TEM and the support, the ceramic thickness increases as here the TE leg length remains fixed. As the ceramic housing consists of materials (Al$_2$O$_3$ and copper) which have a density which is an order of magnitude higher compared to aerogel, as per Table 1, a thickness increase also contributes to the system mass. Thirdly, thicker insulation translates to an expanded RTG volume, thus increasing the overall height of the RTG unit. The fin height is coupled to the height of the RTG, hence it also increases, further contributing to the overall mass increase. Similarly, power is affected by several effects. An insulation thickness increase leads to an increase of the heat flowing through the TEM, $\dot{Q}_{TEM-In}/\dot{Q}_{fuel}$, by ~4 %. Simultaneously, the core RTG temperatures at the outer aeroshell surfaces, and thus T_h, are driven by both the thermal resistance of the bypass branch and by $\dot{Q}_{By}$. The increased thermal resistance of the bypass branch as the insulation thickness increases counteracts the slightly reduced $\dot{Q}_{By}$ fraction and leads to higher ELHS core temperatures, as well as T_h which increases by 9.2 K. On the TEM branch, T_c reduces by 2.3 K despite the increased $\dot{Q}_{TEM-In}$ (and thus $\dot{Q}_{TEM-Out}$) due to the increased radiative surface area and hence reduced thermal resistance of the fins. The increasing ΔT_{TEM}, as well as the increased $\dot{Q}_{TEM-In}$, increase the power output of the RTG. However, the power increase is smaller than the mass increase beyond a certain insulation thickness, leading to the observed non-monotonous behavior.

In contrast to the effect of the aerogel insulation, increasing the hull thickness above 2 mm, which is the final value chosen by the GA, has a detrimental effect on the specific power, as it increases the mass of the RTG considerably without having a visible benefit on the power production (not shown here). This is reasonable as the hull structure does not offer any insulating effects due to the high thermal conductivity of the utilized material. With those relationships now examined, it can be understood that the GA chose to increase the insulation thickness as much as possible while also restricting the hull thickness to its lowest value, allowing the RTG to achieve the maximum possible specific power without T_h exceeding the temperature limit.

The influence of the fin length, L_{fin}, on the specific power, power output and mass of the RTG, as well as on T_h, T_c and $\dot{Q}_{TEM-In}/\dot{Q}_{fuel}$ is seen in Fig. 10. The fin dimensions drive their thermal resistance, which is a combination of conduction resistance (increasing with fin length) and radiation resistance (decreasing with fin length), and thus the temperature distribution on the TEM branch. Increasing the fins' length from 50 to 300 mm considerably reduces their thermal resistance, while the components of the bypass branch kept their original dimensions and hence their original thermal resistance, directing more heat towards the TEM branch by ~6 %. As $\dot{Q}_{By}$ is reduced and the thermal resistance of the bypass branch is kept constant, T_h reduces. Simultaneously, the increased radiative surface area of the fins cools down the RTG more efficiently, resulting in T_c reducing at longer fin lengths. T_c reduces more rapidly compared to T_h, hence ΔT_{TEM} increases and, together with the increased $\dot{Q}_{TEM-In}$, the power output increases as well. However, the benefit of increasing fin length on the power output and on the specific power diminishes as the fin length increases due to the increasing conduction resistance and the decreasing effectiveness of radiative heat transfer with decreasing temperature. Furthermore, the mass increases significantly with increasing fin length. Conclusively, while long fins are
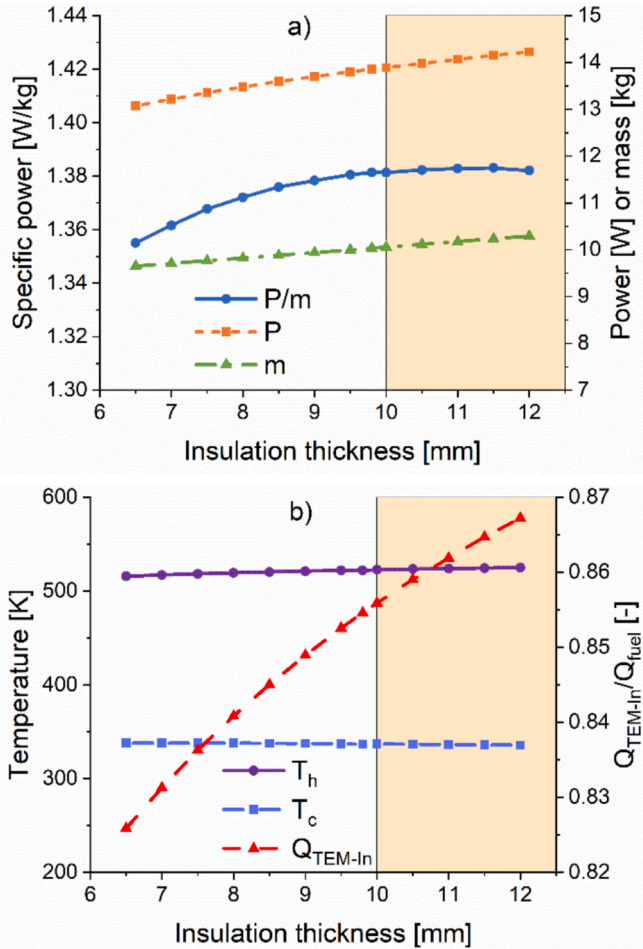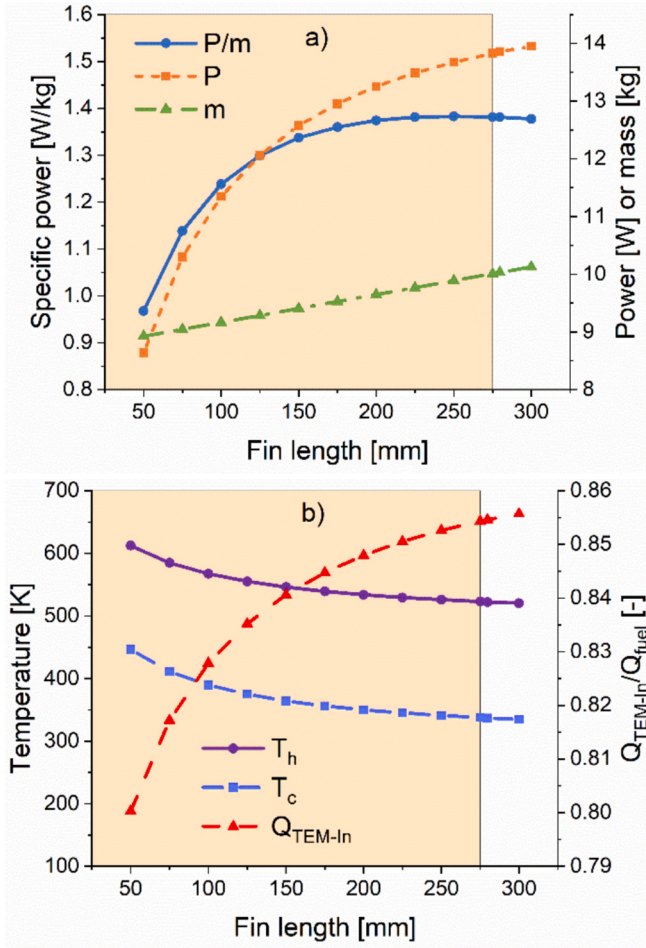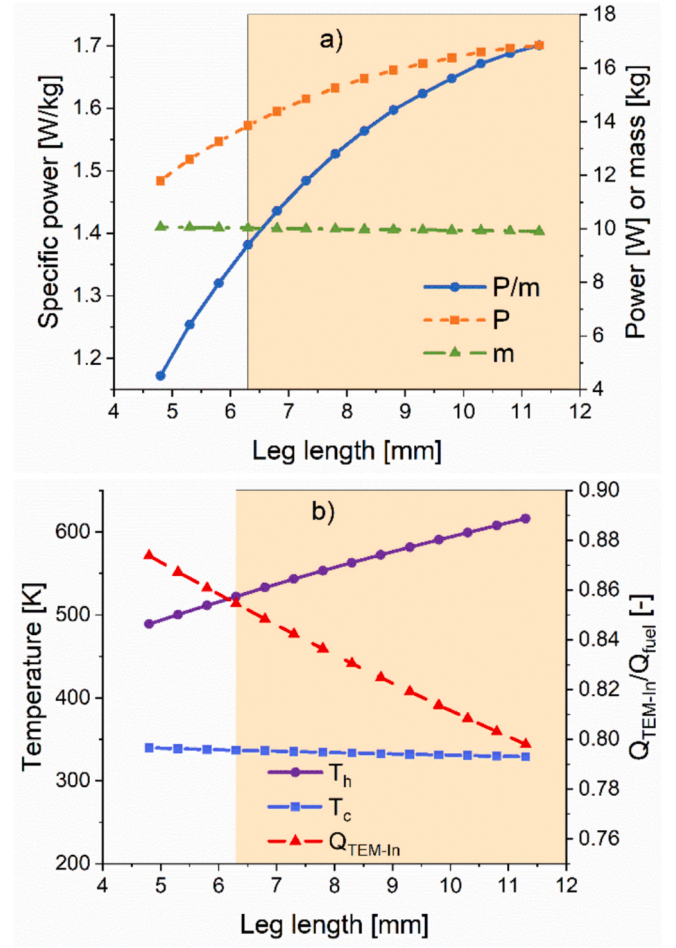
Fig. 10. Impact of fin length on a) specific power, power output and mass of the RTG and b) temperature on the hot and cold junction as well as relative heat flow in the TEM. The shaded region represents the fin length where the safe operating temperature limit of the Bi₂Te₃ TEM, i.e. 523 K, is exceeded.

Fig. 11. Impact of leg length on a) specific power, power output and mass of the RTG and b) temperature on the hot and cold junction as well as relative heat flow in the TEM. The shaded region represents the leg length where the safe operating temperature limit of the Bi₂Te₃ TEM, i.e. 523 K, is exceeded.

necessary to reduce the inner RTG temperatures down to the point where the RTG can be safely operated, a further increase leads to a decrease in the specific power due to the stronger impact on mass compared to power.

The influence of the fin thickness as it changes from 2 to 5 mm is seen in Fig. S6. Increasing the fin thickness has a negative influence on the specific power, decreasing it by 0.1 W/kg, as the RTG mass increases considerably by 1.44 kg without a similar beneficial increase in the power output, which increases by 0.93 W. Consequently, the GA kept the fin thickness low, equal to 2.8 mm, to reduce the system mass while maintaining T_h below its maximum limit. The support thickness, seen in Fig. S7, presents similar trends in all parameters as those produced by the fin length parameter, but at a much smaller magnitude. As the support's thickness increases from 2 to 8 mm, the specific power increases by 0.03 W/kg, reaching a maximum at a thickness of 5 mm which then drops, while the power output and the mass of the system both increase by 0.61 W and 0.26 kg, respectively.

The geometry of the TEM plays a predominant role on the RTG performance. The TEM is characterized by the TE leg length and by the fill factor. To test the influence of the leg length, the housing thickness was changed from 0.5 to 7 mm while the remaining parameters remained equal to those of the optimized geometry from Table 3. This corresponds to a leg length of 11.3 to 4.8 mm, respectively, and its influence is presented in Fig. 11.

Increasing the TE leg length from 4.8 to 11.3 mm increases the thermal resistance of the TEM branch thus reducing $\dot{Q}_{TEM-In}/\dot{Q}_{fuel}$ by

~7.6 %. On the other hand, the temperature difference across the legs is increased, with T_h increasing by 127 K and T_c decreasing by ~11 K at longer lengths. The increase in the bypass heat is responsible for an overall hotter RTG core, hence the increase in T_h, while simultaneously a smaller $\dot{Q}_{TEM-In}$ (and thus a smaller $\dot{Q}_{TEM-Out}$) reduces the magnitude of T_c. Because of the increase in the temperature difference across the legs, the power output and specific power are increased by 5.1 W and 0.53 W/kg, respectively, with the influence of the TE leg length on the mass being negligible and equal to 0.16 kg. For further increasing leg length beyond the limits investigated here, eventually a decrease in the power output is expected because of the reduced $\dot{Q}_{TEM-In}$, thus the optimum leg length is determined by the balance between ΔT_{TEM} and $\dot{Q}_{TEM-In}$. A further trade-off might arise from thermomechanical stresses that are not taken into account in the current model. Thermomechanical stresses are generated at every stage of development of TE materials for space applications, such as fabrication, launch and operation [79,80]. They are caused by different coefficients of thermal expansion in the various components that make up the TEM, by launch vibrations and by compressive loads within the RTG housing [79–83]. The leg length and shape introduce multiple trade-offs regarding their temperature profiles, performance and thermomechanical strength which need to be taken into account holistically [84–87].

Similarly, changing l_{gap} from 1 to 4.5 mm reduces the number of *pn* pairs from 714 to 144, corresponding to a fill factor of 43 % and 8.7 %, respectively. This correlation is presented in Fig. S8 of the ESI. We note that the *p* and *n* legs retained their cross-section area from Table 3 as the

temperature dependence of the optimal cross-section ratio is usually small, as can be seen in Fig. S9 of the ESI. The influence of the fill factor on the RTG performance is presented in Fig. 12.

Reducing the fill factor from 43 % to 8.7 % by correspondingly increasing the gap between legs from 1 to 4.5 mm, considerably reduces the heat passing through the TEM by ~17 %, while also vastly increasing T_h by 277.5 K. Simultaneously, T_c decreases by ~22 K. This increase in ΔT_{TEM} increases the power output by 4.2 W and the specific power by 0.46 W/kg, with the reduction of the number of *pn* pairs from 714 to 144 reducing the RTG mass by 0.35 kg. This small modification in the system mass is reasonable as the TEM accounts for 4.7 % of the total RTG mass as per Fig. 8. Interestingly, both the power output and the specific power present an approximately parabolic profile, with a maximum at a fill factor around 15–12 % (gap between 3–3.5 mm, respectively), which is subsequently decreased at lower fill factors. This corresponds to an adjustment of the thermal resistance of the module with respect to the other elements in this path of the NM: small gaps and high fill factor correspond to large $\dot{Q}_{TEM-In}$ but small ΔT_{TEM} and hence small power, while on the contrary very low fill factors lead inevitably to small $\dot{Q}_{TEM-In}$ (due to the reduced TEM area covered by the thermocouples) and hence small power, despite the large ΔT_{TEM}. This is referred to as the thermal load matching effect, an important optimization factor in TE devices [88]. With the RTG being a closed system, any changes to the design or the boundary conditions in one branch will have a cascade effect in the whole system. Consequently, the increase of the thermal resistance across the TEM branch will inevitably divert more heat towards the bypass branch, leading to a hotter RTG core but also to lower $\dot{Q}_{TEM-In}$ available for power production. The rapid increase in T_h with the reduction in the fill factor quickly drives the TEM temperatures above the safe limits, leading the GA to restrict the fill factor to ~28 %, i. e. gap between the legs of 1.6 mm.

Within the investigated parameter range, the TE leg length, the fill factor and the fin length are the first, second and third most influential parameters, in terms of specific power, respectively. This ranks the TEM as the most critical component out of those studied here for RTG performance, with the fin design being the second most critical component. The latter is further highlighted by the strong impact of the fin thickness, which negatively influences the RTG performance due to its effect on the system mass. Comparatively, the insulation thickness has a smaller influence on the RTG performance, as it primarily increases $\dot{Q}_{TEM-In}$ and T_h. Ranking these parameters based on their impact on the specific power can act as a guideline for future RTG design studies.

Our parametric analysis investigated the leg length and fill factor separately to understand their individual impact. However, in the GA, these parameters are optimized simultaneously as they determine the trade-offs between high $\dot{Q}_{TEM-In}$ and ΔT_{TEM}, and hence power output, while maintaining safe operating temperatures. Both parameters have a strong influence on the thermal resistance of the TEM, which is proportional to the leg length and inversely proportional to the fill factor. A thermal resistance increase will increase ΔT_{TEM} but will, at the same time, increase $\dot{Q}_{By}$, hence there is an optimum thermal resistance for a given RTG system. Thus, for an individual TE module (without considering interface resistances), there are infinite combinations of leg length and fill factor that give the same power output. With respect to the RTG, where the specific power is the optimization target, we find a weak dependence on the ratio of the leg length with the fill factor, l_{TEleg}/FF, presumably mainly due to the interplay of the masses of the TE materials (which increase with increasing leg length but constant l_{TEleg}/FF) and ceramic housing/copper bridges that decrease, resulting in a leg length of 6.3 mm and a fill factor of ~28 %. However, if further effects or boundary conditions are introduced, e.g. electrical contact resistances, radiative bypass through the module, thermomechanical stress or requirements on voltage output, then leg length and fill factor might be decoupled and their optimization results can be largely different.

With the optimized RTG configuration, the model predicts that 171 W_{th}, or ~86 % of the total radioisotope heat, passes through the TEM branch. The temperature at the hot TEM junction reaches 522.1 K, close to the allowed maximum temperature, while the temperature at the cold junction is 336.6 K. Simultaneously, the temperature of the clads is equal to 548.3 K, far below the 1473 K limit mentioned by Ambrosi *et al.* [12]. With a specific power of 1.38 W/kg, the optimized RTG reaches an electrical power output of almost 13.9 W_{el} with an estimated mass of 10.03 kg. This results in a conversion efficiency of 6.93 % for the 200 W_{th} generated by the fuel. The ESA RTG design investigated by Ambrosi *et al.* [12] aimed to achieve a specific power of 1 W/kg with 10 W_{el} and a 5 % conversion efficiency, with their experimental results with a commercial Bi_2Te_3 module showcasing a power output between 9.1–9.3 W_{el}, a system level efficiency of 4.55–4.65 % and a specific power of ~0.99 W/kg. Conclusively, the predicted performance of our optimized RTG exceeds the ESA RTG specifications by far. Part of the explanation is the performed design optimization, which resulted in an increased overall size and particularly longer fin lengths: the diameter (measured from the end of opposite fins) of the optimized RTG is 767 mm, while the design by Ambrosi *et al.* [12] had a diameter of 523 mm. The lack of data for the ESA RTG regarding material specifications, component dimensions, interface resistances and modelling assumptions due to confidentiality reasons, makes it difficult to directly compare our results. Any comparisons between our models and the experimental RTG data will be based on a large number of not well-justified assumptions on various aspects of the RTG design. Consequently, any resemblance of our data
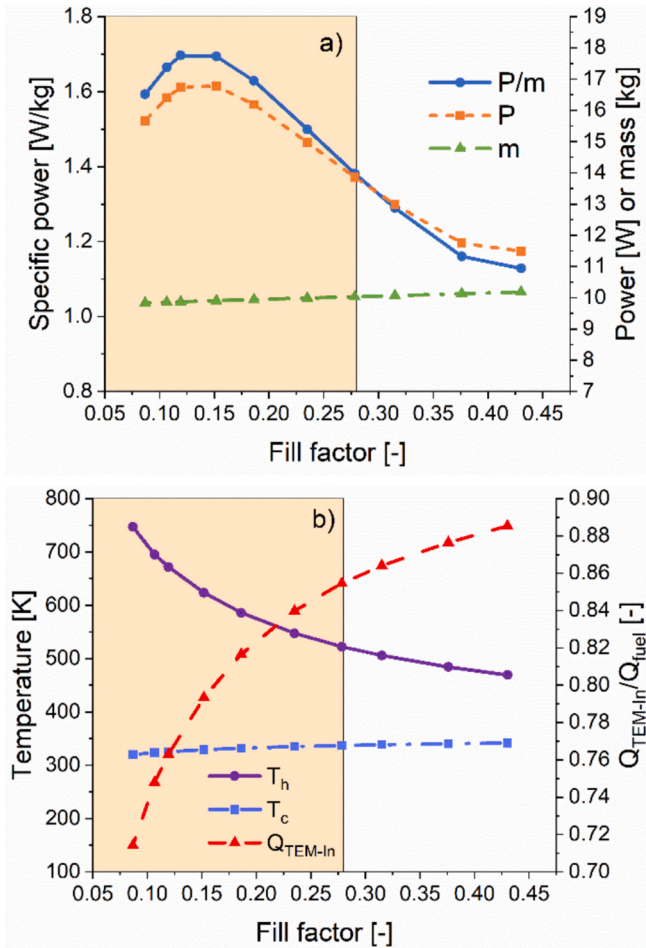

Fig. 12. Impact of the fill factor on a) specific power, power output and mass of the RTG and b) temperature on the hot and cold junction as well as relative heat flow in the TEM. The shaded region represents the fill factor where the safe operating temperature limit of the Bi_2Te_3 TEM, i.e. 523 K, is exceeded.

with the experiments will be purely coincidental, thus offering no value in terms of validation. Once more data on the ESA RTG becomes available, e.g. after it has been flight tested, then this can be used to verify and improve our model's accuracy. Some insight can be gained by including the purely thermal FEA simulations performed by Ambrosi *et al.* [12] which showed that 75 % of total radioisotope heat passed through the TEM [12]. Drawing direct comparisons between their thermal simulations and our TE simulations, which indicate an approximate thermal efficiency of 86 %, would lead to misleading conclusions, since, as discussed in the next section, TE effects strongly influence the temperature and heat flux distributions. However, we have also run our NM at OC conditions, completely neglecting all TE phenomena. Our OC simulations indicate a thermal efficiency of ~81 %, which is a considerable increase over the 75 % thermal efficiency reported by Ambrosi *et al.* [12]. Two further points need to be taken into account in that comparison: first that the thermal boundary conditions are not exactly the same (they are not clearly defined in the work from Ambrosi *et al.* [12]) and second that our NM neglects a few loss mechanisms (electrical interface resistances, radiation through the TEM, etc.) which will inevitably reduce the performance to a small extent.

3.2. Model validation with FEA results

To validate the accuracy of the NM, it is compared with our two 3D FEA axisymmetric models utilizing the optimized geometry of Table 3. In the FEA models, the temperatures of the various components were calculated as surface-averaged temperatures (at the outer, cold surface), with the exception of the fuel pellet where the core temperature in the center of the pellet is compared. In addition, the $P(I)$ curves of the models were calculated and compared. The decoupled FEA case, where the TEM and bypass branches are thermally decoupled, i.e. replicating the NM approach, is labelled simply as "3D", while the FEA case where heat exchange is enabled between the two branches is labelled as "3D HEx". The temperature comparison for all components at the current for maximum power, 0.66 A, is presented in Fig. 13a, while the comparison of the P-I curve is presented in Fig. 13b. The performance of the RTG when operated at the current for maximum power, as calculated from the NM and the 3D models, is presented in Table 4. The voltage predicted by the models as a function of current, as well as the temperatures at the hot and cold junction, are presented in Fig. S10.

When comparing the NM with the "3D" case at the current for maximum power, Fig. 13a, all temperature predictions are very close, with an average error of 1.1 %. The largest error is observed in the prediction of the temperature at the fuel core, i.e. in the center of the fuel pellets, where the network model predicts 2.3 % higher temperatures compared to the 3D. As described in Eqs. (5) and (6), the network model solves the Fourier heat transfer equation coupled with heat generation. These equations, however, do not account for the heat flowing at the top and bottom of the Am pellet and we account for this approximately by reducing the portion of the total heat flowing through the surface by introducing the geometry factor, α_{GF}, hence neglecting the vertical temperature gradient. The small magnitudes of the deviations in the predictions of the two models are further confirmed by the temperature profiles across the fin length, shown in Fig. S11, which are almost identical. By examining the "3D HEx" case, we can see that practically all inner temperatures until the outer aeroshell surface and the hot TEM surface are identical to those predicted by the "3D" case, hence presenting the same small differences compared to the NM. The differences start from the cold TEM side and moving outwards, with the components of the TEM branch, i.e. cold TEM side, support and fins (Fig. S11), being the warmest and the components in the bypass branch, i.e. insulation and hull, being the coldest in the "3D HEx" case. Due to the larger area and larger emissivity of the fins compared to the hull, a significant fraction of the heat that corresponds in the decoupled case to $\dot{Q}_{By}$ flows through the cold ceramic of the TEM and the support towards the fins,
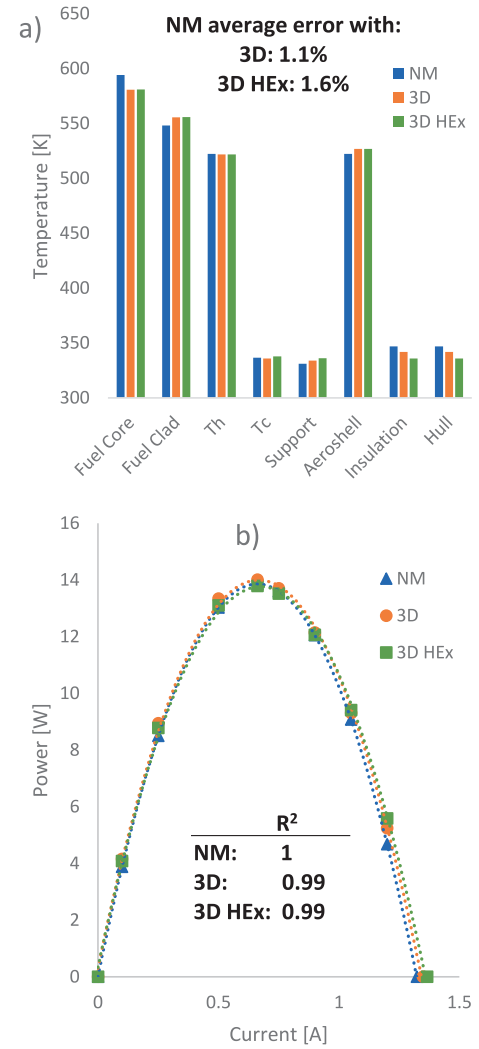
Fig. 13. Comparison of a) average temperatures at the outer surfaces of the RTG components and at the core of the fuel pellet, for an RTG operating at the optimum current for maximum power, and b) P-I curve of the network model (NM) and 3D models. Two 3D FEA models are considered, the "3D" case, which decouples the TEM and bypass branches, thus replicating the NM approach, and the "3D HEx" case, where heat exchange between the two branches is enabled. The NM showcases an average error of 1.1% and 1.6% at the temperature profiles with respect to the "3D" and "3D HEx" cases, respectively, achieving an excellent accuracy. Similar accuracy can be observed across all ten current values (and hence RTG states) calculated to generate the P-I curve and all models agree on the peak of the P-I curve and thus on the optimum current.

Table 4
Performance of the RTG when operated at the current for maximum power output, as calculated by the network model and the two 3D models. By comparing the NM with the "3D" case, it can be concluded that the geometrical simplifications made by the NM introduce minor errors in the TE performance compared to the 3D FEA model. By comparing the NM with the "3D HEx" FEA model, we can see that $\dot{Q}_{TEM-Out}$, which corresponds here to the heat flowing into the fins, is now higher, as heat moves from the hull through the support and towards the fins.

	Network model	3D	3D HEx
$\dot{Q}_{TEM-In}$	170.9 W_{th}	171.5 W_{th} (0.3 %)	171 W_{th} (0.0 %)
$\dot{Q}_{TEM-Out}$	157.3 W_{th}	157.4 W_{th} (0.2 %)	162.1 W_{th} (3.1 %)
$\dot{Q}_{By}$	29.1 W_{th}	28.7 W_{th} (1.3 %)	29 W_{th} (0.2 %)
P_{TEM}	13.9 W_{el}	14 W_{el} (1.1 %)	13.8 W_{el} (0.5 %)
η_{RTG}	6.9 %	7.0 % (1.4 %)	6.9 % (0.5 %)

hence increasing the temperatures of these components but decreasing the temperature of the insulation and the hull. This effect also takes place in the hot side, however because there the temperatures between the two branches are much closer, its magnitude is much weaker. For ease of comparison, we have added this heat flow between the branches to $\dot{Q}_{\text{TEM-Out}}$, which corresponds to the heat flowing into the fins (identical to the heat flowing out of the TEM in the decoupled case), increasing it by ~ 5 W$_{\text{th}}$, as seen in Table 4. The temperature inhomogeneities at the hot and cold TEM junctions, predicted by the "3D" and "3D HEx" cases are presented in Fig. S12 and S13 of the ESI, respectively. These temperature inhomogeneities are in the order of 2–3 K for both cases, justifying the assumption to approach them as a homogeneous temperature in the NM.

When the RTG performance is investigated, Table 4, a similarly low deviation is observed. Specifically, the network model has a 0.3 % deviation with respect to the heat passing through the TEM, and a 1.1 % deviation in the predicted power generation compared to the "3D" case. Compared to the "3D HEx" case, the NM has an even smaller error at $\dot{Q}_{\text{TEM-In}}$, power output and efficiency and a slightly larger error, equal to 3.1 %, at $\dot{Q}_{\text{TEM-Out}}$. All three models also achieve excellent agreement across the entire P-I curve, Fig. 13b, with the "3D" case overall predicting a slightly higher electrical power output and the "3D HEx" case predicting a slightly lower power output compared to the NM, because of the reduced ΔT_{TEM} from the heat exchange. Similar conclusions can be reached by examining the voltage, T_h and T_c parameters as a function of the current, Fig. S10. The NM and "3D" models show a good agreement in all three profiles. The largest deviations can be observed at the smallest, <0.25 A, and largest currents, >1.2 A, but even in these cases the differences in the power production do not exceed 0.6 W. However, while the "3D HEx" case has an almost identical T_h profile with the "3D" and NM cases, its T_c deviates from the profiles of the other two cases. As will be discussed later, smaller currents are associated with a larger $\dot{Q}_{\text{By}}$ and thus a larger portion of this heat flowing to the cold TEM side, locally increasing T_c. At higher currents, the T_c predicted by the "3D HEx" case is lower than those predicted by the NM and "3D" cases (Fig. S10c). Interestingly, because of a larger $\dot{Q}_{\text{TEM-In}}$ for higher currents, T_c is higher than the local hull temperature at the interface, and now heat moves from the ceramic towards the hull. Subsequently, as the outer support surface and fins are at a lower temperature than the outer hull surface, a portion of this heat then flows towards the fins. It should also be noted that $P(I)$ can be well approximated by a parabola, with NM, "3D" and "3D HEx" cases all having an R^2 value of 1, 0.99 and 0.99, respectively. While when operating a TEM at a constant T_h and T_c an almost perfectly quadratic behavior is expected and observed with changing current, one should note that in the RTG system T_h and T_c change significantly as a function of current, as per Fig. S10, so a quadratic dependence is not necessarily expected. While the 3D FEA results in Fig. 13 validate the NM for 10 different operating currents, it is also important to verify the agreement between NM and FEA for geometries away from the optimum to ensure that the optimization by the GA works correctly. For this, we performed a parametric study around the GA-produced optimum with our de-coupled FEA model, i.e. the "3D" case, where the fin length changed from 50 to 300 mm, i.e. following the results from Fig. 10. The FEA and NM comparative results for power output, $\dot{Q}_{\text{TEM-In}}$, T_h and T_c are presented in Fig. S14 of the ESI. It can be seen that the FEA yields the same trends for all four parameters with relative differences < 1.5 %, further reinforcing that our NM correctly captures the FEA behavior. As the influence of heat exchange between the two branches has been quantified, all discussions henceforth will compare the NM with the "3D" case because of their identical approach to the branch coupling, hence allowing us to estimate in-depth the errors observed in the NM results.

Understanding the reason for these differences is key for model improvement. Therefore, the NM and "3D" models' results at $I = 0$ have been examined, because in this condition all TE phenomena are neglected and the influence of the methodological approach, as well as of the geometric differences between the two models, can become apparent. At $I = 0$, the network model predicts both a lower T_h and a lower T_c by 2.3 and 1.5 K, respectively, compared to the 3D model. This translates into a ΔT_{TEM} of 255.8 K and 255 K for the 3D and NM, respectively. However, $\Delta T'_{\text{TEM}}$, which drives the TE performance, is determined by the influence of the TEM housing (ceramic and copper connections). The 3D model considers the ceramic layer and the copper connections separately. The latter have a higher thermal conductivity but a reduced surface area, dependent on the fill factor of the TE legs, thus introducing a constriction effect on local heat transfer. On the other hand, in the network model, only a single combined resistor is considered with the thermal conductivity of the ceramic, the area of the TEM and a thickness corresponding to the sum of Cu and ceramic. As a result, a different temperature change is introduced by the TEM housing between the two models. Specifically, $\Delta T'_{\text{TEM}}$ is equal to ~ 253.9 K and ~ 252.7 K for the 3D and NM, respectively, corresponding to a temperature change of 0.95 K (3D) and 1.15 K (NM) in each side of the ceramic, which explains the higher voltage prediction of the 3D model seen in Fig. S10a.

Beyond the influence of the ceramic on the inner TEM temperatures, when a current is introduced in the 3D model, the copper bridges generate heat due to the Joule effect which introduces a small local heat source in the 3D model which is not taken into account in the NM. In addition, because of the temperature-dependency of copper's electrical resistivity, Fig. S2 in the ESI, the Joule heating in the hot side will be stronger than that at the cold side, thus raising T'_h more than T'_c and further increasing $\Delta T'_{\text{TEM}}$. The influence of the ceramic and the copper result in the 3D model having an overall higher electrical power output and voltage prediction than the NM. However, as can be seen in Fig. S15, the total Joule heat is much smaller compared to the Fourier and Peltier heat flows, thus the effect from the Joule heating of the Cu bridges is presumably small.

The agreement between the two models also reinforces the potential of the NM to be used as an analysis tool to interpret the various TE terms involved in the operation of the RTG. Both models agree on the temperature changes in the hot and cold TEM junction as the current changes, Fig. S10. Specifically, due to the absorbed Peltier heat, proportional to the current, $T_h(I)$ follows a linear drop as current increases while $T_c(I)$ reaches a minimum at a current of around 0.5 A and increases afterwards. Both temperatures are directly related to the respective heat flow at the hot and cold junctions, $\dot{Q}_{\text{TEM-In}}$ and $\dot{Q}_{\text{TEM-Out}}$, respectively, and their association with the electrical power output. This coupling is presented in Fig. S15a of the ESI. Because of the linear increase in $\dot{Q}_{\text{TEM-In}}(I)$ and the parabolic profile of $P_{\text{TEM}}(I)$ as current increases, $\dot{Q}_{\text{TEM-Out}}(I)$ presents an initial drop to a minimum at a current of around 0.5 A, followed by a subsequent increase. As temperatures in all components past the TEM cold side are driven by $\dot{Q}_{\text{TEM-Out}}(I)$, this corresponds to the minimum observed in $T_c(I)$ for the same current. Simultaneously, both the Peltier and the Joule terms contributions keep increasing at higher currents while the Fourier term keeps decreasing. Specifically, at the hot TEM side, Peltier contribution exceeds the Fourier contribution at a current slightly above 1 A while the Joule term is considerably smaller compared to the other two terms, as seen in Fig. S15b. For the TEM's cold side, Fig. S15c, a similar behavior is observed, however, here the Peltier term does not reach the Fourier term even at the highest currents considered.

It is not only the excellent accuracy of the NM with respect to the 3D model results that makes it a valuable tool but also the considerable gain in the computational resources. These are presented in Table 5, which shows the computational resources to run the GA optimization, as well as to simulate the optimized RTG geometry with the NM and 3D model (single case). The NM and GA cases were simulated on a 13th Generation Intel® i7 processor with 1.7 GHz and 16 Gb of RAM, while the 3D FEA case was simulated on 36 Intel® Xeon® processors with 3.0 GHz,

Table 5

Computational resource demands for the calculations performed by the different models. Within the 3.2 sec, the NM calculates four RTG states to derive the optimum current, which makes it three orders of magnitude faster compared to the 3D FEA model which calculates a single RTG case in 826 sec.

	Computational time	RAM	File size
NM – GA optimiz.	21 h	11.9 Gb	580 Mb
NM – single case	3.17 sec	0.2 Gb	1.4 MB
3D FEA – single case	826 sec	28 Gb	580 Mb

utilizing 512 Gb of RAM. We note that the "3D HEx" case had similar but slightly higher computational resource demands as the "3D" case.

The computational resources are vastly different. The NM requires on average 260 times less computational time for a single geometry, compared to the 3D model. However, it should furthermore be noted that within a single NM run the RTG performance for four operating currents is calculated (three to produce the $P(I)$ curve and determine the optimum operating current for the fourth, optimized RTG state). Instead, the 3D single case doesn't contain the current variation and is operated directly at the optimum current calculated by the NM, essentially making the NM three orders of magnitude faster. Moreover, the NM utilizes 140 times less RAM and 414 times less storage size, making it easier to handle and to store data in a normal personal computer. On the contrary, the 3D case requires a dedicated workstation to solve and to process. Because of the stark reduction in the computational resources achieved by the NM, utilization of the GA becomes possible. With the need to solve 70 k cases during its optimization task, coupling of the GA with the NM becomes the only reasonable approach as a coupling with the 3D FEA model would make the computational costs prohibitively expensive.

The above comparison between the two models clearly showcases that the geometrical simplifications of the NM, which represents the RTG structure as a serial-parallel TE network, introduce minor deviations in the results. Moreover, we also showcased the differences introduced when heat exchange is enabled between the two thermal branches and found only minor differences in the temperature profiles and power output, further justifying that our NM, despite its simplifications and lack of the heat exchange terms, is not far from reality. The overall low error of the NM in the temperature profiles and the TE performance with the "3D" case of around 1.1 %, coupled with three orders of magnitude reduction in the computational time, gives evidence that this approach could be highly valuable, acting as a solid foundation to further refine the NM to better represent reality and allow for more realistic case studies. Utilizing the same assumptions and operating regimes in our NM and "3D" models enabled us to analyze in-depth differences introduced by translating the complex, truncated-triangle 3D ESA RTG geometry into a one-dimensional model. Here, we presented and validated our tools in an ideal scenario, with no interface resistances or degradation phenomena. Subsequent steps to bring the NM closer to reality would be to introduce a thermal coupling between the two branches, a thermal bypass within the TEM (either radiative or conductive if thermal insulation within the TE module is considered), introduce support radiation and introduce interface resistances, both thermal (within the TE module but also between different components of the RTG) and electrical (within the TEM). Heat exchange between the two here separate paths can be considered by including additional resistances in the NM and modify the heat balance equations by adding coupling terms. The exchanged heat will depend on the temperature differences and the thermal resistance of the path, which in turn depends on the geometry of the coupling elements, their thermal conductivities as well as the interface characteristics, i.e. area and thermal resistance, with the latter to be determined experimentally. If those are known, the system can be solved similarly as done now.

While validation with experimental data is key in any paper focusing on model development, RTG literature has a lot of sensitive information which creates similar challenges as faced here for the ESA RTG. On the Chinese Chang'E-4 RTG [39], researchers try to validate their FEA model with laboratory experiments, however details about the cooling flow loop used at the fins during the experiments to represent ambient conditions were not disclosed, leading the researchers to make several assumptions for the operating boundary conditions [39]. For NASA's RTGs, while NASA-related researchers have been able to benchmark their models [36,37], results and details about their model setup are not made publicly available, as it consists of over 200 parameters most of which are mission specific [89], leading independent researchers to a number of assumptions to setup their models [7,40]. As such, while RTG-specific data are expected to remain sensitive, alternative experimental setups, such as electrical analogues to test TEM degradation [34], or mechanical analogues to simulate the high-frequency vibrations expected during launch [90], are expected to fill the missing data gap. Introducing further phenomena and experimental parameters in our models, based on experimental campaign data, to increase physical accuracy will shift the predicted power output of the optimized RTG showcased here. For example, support radiation will enhance RTG cooling and hence performance, while thermal and electrical contact resistances, thermal bypass in-between the TE legs, and view factors at the fins will all reduce performance. Estimating the magnitude of these changes can help re-design the RTG to mitigate them. In addition, by comparing the "3D" and "3D HEx" results, it can be seen that allowing heat exchange at the cold TEM interface with the insulation/hull reduces ΔT_{TEM} and thus power output for the considered case. Hence, studying where thermal decoupling is beneficial would guide further optimization of the RTG.

In this study, optimization focused on maximizing the specific power of the RTG, along with restrictions on the temperature at the TEM's hot side and at the fuel cladding. Coupling of the GA with the NM allows the rapid re-optimization of the RTG geometry based on various mission-relevant scenarios. This is possible by accommodating further criteria that can arise from RTG handling and utilization, as will be the case during the establishment of a lunar base. An example of a scenario that could be examined in the future is the variation of the environmental temperature on the lunar surface during the lunar day-night cycle, which was assumed constant here. With the surface temperature ranging between 100 K (lunar night) and 400 K (lunar day) [8], the power output of the RTG, as well as its inner temperatures, could deviate significantly from the results seen here, potentially increasing the core temperatures beyond safe operating limits. To evaluate this, future studies will investigate the magnitude of the influence of the environmental temperature on the TE performance, as well as the risk of overheating. With the lunar day-night cycle lasting ~28 Earth days, investigating different environmental temperatures in a quasi-steady-state-approach as feasible by the presented approach is a reasonable strategy. The influence of solar irradiation on exposed RTG surfaces could be another key phenomenon. Solar exposure for the extended duration of the lunar day could overheat some RTG components (in particular the TEM), accelerating degradation. Such phenomena could introduce additional restrictions on RTG design, requiring re-optimization, shading strategies, as proposed by [37] and [8], or the selection of alternative materials or of coatings, which can easily be done with our method. All these effects would require a more detailed implementation of radiation on the outer RTG surface (surface-to-surface radiation, view factors, etc.) to correctly represent an RTG operation on the lunar surface. Approximately, these effects can be captured in the NM by considering e.g. effective view factors for the fins and/or splitting the two currently used branches into multiple with the addition of heat source terms in some of them, representing the inhomogeneous exposure of the outer RTG surface, determined by the incident angle of the sun. On the other hand, radiation-related phenomena can be introduced accurately in the FEA model, taking advantage of its 3D and ray-tracing capabilities. The coupling of the FEA model with our NM creates a framework that could

analyze the RTG behavior in-depth for various mission scenarios and propose adjustments or re-optimization. A further point to consider are degradation phenomena of the RTG, which are key considering missions that deploy RTGs have an expected duration of > 15 years. Consequently, optimization of RTGs should not only focus on beginning-of-life performance, but also on end-of-design-life (EODL) or on the lifetime performance. Our tools could be used to estimate the influence of various phenomena that would alter the heat distribution within the RTG, as well as phenomena associated with degradation. For example, reducing the heat generation of the ^{241}Am pellets could approximate the radioactivity loss from the isotope's half-life. By reducing the materials' TE properties or by increasing the thermal and electrical resistances, based on available experimental data, the TEM degradation could be approximated.

Another key aspect of the RTG utilization is its operating voltage. NASA's MMRTG can accommodate a voltage range in-between 22–36 V [36], however it is ideally designed to operate at 28 V. This is the voltage chosen for the two Mars rovers operation [91,92], as well as the voltage that the upcoming Lunar rover, Volatiles Investigating Polar Exploration Rover (VIPER), would operate at if a radioisotope power system is chosen as its power source [93]. In our investigation, we did not consider a criterion for the operating voltage. As such, the optimized RTG, when operated at its optimum current for maximum power, has a voltage of 21 V. The user of the RTG can choose to operate it at a different voltage level, according to the electrical resistance of the connected load. However, it becomes apparent from Fig. S10 that changing the voltage level changes the TEM's hot side temperature dramatically. Specifically, T_h changes by ~116 K (NM prediction) or 119 K (3D model prediction) as voltage changes from its OC value to its SC value. From Fig. S10 it can be understood that higher voltages correspond to lower currents and reduced Joule and Peltier heating, leading to reduced $\dot{Q}_{\text{TEM}-\text{In}}$ and higher T_h. This explains the observation of Whiting *et al.* where higher operating voltages led to elevated internal temperatures on the MMRTG [37]. Consequently, depending on the application of the technology, the user needs to consider how the RTG's operating regime will affect the T_h magnitude and whether it will exceed the TEM's safe operating temperatures. In addition, the RTG studied here is a single unit with a power output of ~14 W_{el}. Stacking multiple units together to increase the power output would require adjustment of the system voltage. DC-DC converters could be employed, although such an approach could introduce risks as they will increase the system mass, reduce the efficiency and add system complexity. Our results also agree with the conclusion reached by Liu *et al.* [40] who identified that during transport, keeping the RTG at short-circuit mode is preferable as T_h is minimized thus preventing damage to the TE modules.

Alternative TEM could also be investigated. The Stirling-based power system of Mesalam *et al.* [24] which uses four ELHS instead of the one considered here was estimated to nominally produce 216 W_{el} with a specific power of 1.96 W/kg and a thermal-to-electricity conversion efficiency of 28 %. However, the temperature at their hot junction was at 973 K, which is almost double the temperature considered for Bi_2Te_3. Our model can be used to adapt the RTG design to utilize novel TEM with higher operating temperatures, such as Half-Heusler (750 K), Skutterudites (873 K) or SiGe (1273 K), which could potentially match the specific power of the Stirling-based power system. This could be highly beneficial as the reliability, longevity and relative simplicity in operation of the RTGs could allow them to fill technological gaps that Stirling-based systems might be unsuitable for, thus the two technologies could co-exist in a future space economy.

Regardless of the application scenario, our developed tools are suitable to investigate and re-optimize the RTG. Expanding the GA optimization to introduce additional constraints, inspired by stakeholder requirements or for specific missions, can easily be done. The flexibility and applicability of our models allow them to guide RTG design for any mission scenario, accelerating its TRL and advancing its status for deployment.

4. Conclusions

NASA has a long history of deploying Radioisotope Thermoelectric Generators (RTGs) to power their missions where solar availability is scarce, such as the Voyager probes or the Curiosity rover. During such missions, RTGs have proven their reliability and longevity. Simultaneously, ESA is currently funding the development of its own 200 W_{th}-10 W_{el} RTG unit. RTGs consist of a multitude of functionally interlinked components. In its core, multi-layer containment measures are used to prevent fuel leakage. Thermoelectric modules, placed in contact with the RTG core, are responsible for electrical power output and should thus be designed to maximize their performance. Thermal insulation, surrounding the free areas of the RTG core, aim to drive the majority of the heat through the thermoelectric modules. Optimizing the RTG design and maximizing its specific power is a complex multi-disciplinary challenge and requires multi-parametric design tools, capable of in-depth investigations of all design parameters.

Here we present a thermoelectric network model, coupled with a genetic algorithm tool, which simulates the RTG as two independent heat transfer branches. Using an iterative process, the model then calculates the heat flowing through the thermoelectric module, responsible for power generation, and through the bypass branch, which accounts for heat losses through the insulation. Based on the heat flow in these two branches, the temperature difference across each RTG component can be calculated, necessary to evaluate the thermoelectric performance. A design optimization performed by the genetic algorithm maximized the specific power of the RTG while maintaining the component temperatures within safe operating limits. The optimized RTG is estimated to have a specific power of 1.38 W/kg, with an electrical power output of 13.9 W_{el} and a conversion efficiency of 6.9 %, a considerable increase over the pre-defined ESA specifications of 10 W_{el}, 1 W/kg and a conversion efficiency of 5 %. Comparison of our model with a 3D Finite Element Analysis model showed an excellent accuracy with an average error of around 1.1 % and with considerably reduced computational resources. Our tools can be used for further optimization studies to accelerate the technology readiness level of RTGs for ESA, preparing them for mission deployments.

CRediT authorship contribution statement

Stylianos Kyrimis: Writing – review & editing, Writing – original draft, Visualization, Validation, Methodology, Investigation, Funding acquisition. **Eliott Lallemand:** Writing – original draft, Validation, Methodology, Investigation. **Christian Stiewe:** Writing – review & editing, Methodology. **Pawel Ziolkowski:** Writing – review & editing, Supervision, Methodology, Investigation. **Aidan Cowley:** Supervision. **Eckhard Müller:** Writing – review & editing, Supervision, Methodology, Investigation, Funding acquisition. **Johannes de Boor:** Writing – review & editing, Writing – original draft, Visualization, Validation, Methodology, Investigation, Funding acquisition, Supervision.

Declaration of competing interest

The authors declare that they have no known competing financial interests or personal relationships that could have appeared to influence the work reported in this paper.

Acknowledgements

agreement No 101209597, as well as from the German Academic Exchange Service (DAAD). E.L. received financial support by the European Astronaut Centre of the European Space Agency, making this study possible thank to the Spaceship EAC initiative.

Appendix A. Supplementary data

Supplementary data to this article can be found online at https://doi.org/10.1016/j.ecmx.2025.101395.

Data availability

Data will be made available on request.

References

[1] J. Clark *et al.*, "Assessing the full effects of public investment in space," *Space Policy,* vol. 30, no. 3, Part A, pp. 121-134, 2014/08/01/ 2014, doi: doi:10.1016/j.spacepol.2014.03.001.

[2] Creech Steve, Guidi John, and E. Darcy, "Artemis: An Overview of NASA's Activities to Return Humans to the Moon," presented at the IEEE Aerospace Conference 2022, US, March 2022, 2022.

[3] Crawford IA. The long-term scientific benefits of a space economy. Space Policy 2016;37:58–61. https://doi.org/10.1016/j.spacepol.2016.07.003.

[4] Sommariva A, Gori L, Chizzolini B, Pianorsi M. The economics of moon mining. Acta Astronaut 2020;170:712–8. https://doi.org/10.1016/j.actaastro.2020.01.042.

[5] European Space Agency (ESA). "ESA budget 2024." https://www.esa.int/ESA_Multimedia/Images/2024/01/ESA_budget_2024 (accessed.

[6] National Aeronautics and Space Administration (NASA), "FY 2024 Budget Estimates," 2024.

[7] Tailin L, Youhong L, Yingzeng Z, Haodong C, Qingpei X. Comprehensive modeling and characterization of the general-purpose heat source radioisotope thermoelectric generator for solar system missions. Appl Therm Eng 2024;248: 123278. https://doi.org/10.1016/j.applthermaleng.2024.123278.

[8] C. Barklay, C. Whiting, P. Schmitz, and T. Sutliff, "Can MMRTG Operate on the Moon? Insights from SNAP-27 for Apollo Lunar Surface Experiment Package," in *2021 IEEE Aerospace Conference (50100)*, 6-13 March 2021 2021, pp. 1-6, doi: 10.1109/AERO50100.2021.9438465.

[9] Christopher J. Wohl *et al.*, "Lunar Dust Considerations for Vertical Solar Arrays Volume 1: Lunar Environment and Dust Interactions," National Aeronautics and Space Administration (NASA), 2024.

[10] A. J. Zillmer, "The History of the United States's Flight and Terrestrial RTGs," in *The Technology of Discovery*, 2023, pp. 7–33.

[11] Y. H. Lee and B. K. Bairstow, "US Space Flights Enabled by RTGs," in *The Technology of Discovery*, 2023, pp. 35–75.

[12] Ambrosi RM, et al. European radioisotope thermoelectric generators (RTGs) and radioisotope heater units (RHUs) for space science and exploration. Space Sci Rev 2019;:215(8):55. https://doi.org/10.1007/s11214-019-0623-9.

[13] M. B. Naseem, J. Lee, and S.-I. In, "Radioisotope thermoelectric generators (RTGs): a review of current challenges and future applications," *Chemical Communications,* 10.1039/D4CC03980G vol. 60, no. 96, pp. 14155-14167, 2024, doi: 10.1039/D4CC03980G.

[14] T. Tinsley, M. Sarsfield, K. Stephenson, and R. Ambrosi, "Progress and future roadmap on 241Am production for use in Radioisotope Power Systems," in *2019 IEEE Aerospace Conference*, 2-9 March 2019 2019, pp. 1-8, doi: 10.1109/AERO.2019.8741817.

[15] Ambrosi RM, Kramer DP, Watkinson EJ, Mesalam R, Barco A. A concept study on advanced radioisotope solid solutions and mixed-oxide fuel forms for future space nuclear power systems. Nucl Technol 2021;:207(6):773–81. https://doi.org/10.1080/00295450.2021.1888616.

[16] C. Barklay, D. Kramer, R. Ambrosi, and R. Mesalam, "Development Concept for a High-Efficiency Cascaded Thermoelectric Radioisotope Power System," in *2019 IEEE Aerospace Conference*, 2-9 March 2019 2019, pp. 1-6, doi: 10.1109/AERO.2019.8741527.

[17] Dustin JS, Borrelli RA. Modeling of Am-241 as an alternative fuel source in a radioisotope thermoelectric generator. Nucl Eng Des 2021;385:111495. https://doi.org/10.1016/j.nucengdes.2021.111495.

[18] Dustin JS, Borrelli RA. Assessment of alternative radionuclides for use in a radioisotope thermoelectric generator. Nucl Eng Des 2021;385:111475. https://doi.org/10.1016/j.nucengdes.2021.111475.

[19] C. Fongarland *et al.*, "Overview of the issues related to the use of Radioisotope Power Systems in European space missions," in *2019 European Space Power Conference (ESPC)*, 30 Sept.-4 Oct. 2019 2019, pp. 1-5, doi: 10.1109/ESPC47532.2019.9049264.

[20] C. Barklay, E. J. Watkinson, R. Ambrosi, R. Mesalam, A. Barco, and D. Kramer, "Considerations for Utilising Alternative Radioisotopes in Radioisotope Power Systems," in *2021 IEEE Aerospace Conference (50100)*, 6-13 March 2021 2021, pp. 1-6, doi: 10.1109/AERO50100.2021.9438353.

[21] M. B. R. Smith *et al.*, "Nuclear Physics, Radioisotope Fuels, and Protective Components," in *The Technology of Discovery*, 2023, pp. 85-132.

[22] A. Barco, C. Fongarland, R. M. Ambrosi, M. Libessart, and K. Stephenson, "Safety Studies for the ESA Space Nuclear Power Systems: Accident Modelling and Analysis," in *2019 IEEE Aerospace Conference*, 2-9 March 2019 2019, pp. 1-8, doi: 10.1109/AERO.2019.8741744.

[23] Barco A, Ambrosi RM, Fongarland C, Brunet P, Guguin Y, Stephenson K. Impact tests and modelling for the ESA radioisotope power systems. J Space Safety Eng 2022;9(1):56–71. https://doi.org/10.1016/j.jsse.2021.11.001.

[24] Mesalam R, et al. Americium fuelled radioisotope stirling generator for lunar surface mobility systems. Acta Astronaut 2025;228:331–45. https://doi.org/10.1016/j.actaastro.2024.12.001.

[25] G. J. Snyder, "Thermoelectric Energy Harvesting," in *Energy Harvesting Technologies*, S. Priya and D. J. Inman Eds. Boston, MA: Springer US, 2009, pp. 325-336.

[26] Snyder GJ, Toberer ES. Complex thermoelectric materials. Nat Mater 2008;7(2): 105–14. https://doi.org/10.1038/nmat2090.

[27] C. E. Whiting and D. F. Woerner, "Lifetime Performance of Spaceborne RTGs," in *The Technology of Discovery*, 2023, pp. 183-212.

[28] Jouhara H, et al. Thermoelectric generator (TEG) technologies and applications. Int J Thermofluids 2021;9:100063. https://doi.org/10.1016/j.ijft.2021.100063.

[29] C. E. Whiting, M. B. R. Smith, and T. Caillat, "Modern Analysis Tools and Techniques for RTGs," in *The Technology of Discovery*, 2023, pp. 213–243.

[30] Duparchy A, et al. Instability mechanism in thermoelectric Mg2(Si,Sn) and the role of Mg diffusion at room temperature. Small Sci 2024;:2300298. https://doi.org/10.1002/smsc.202300298.

[31] A. Duparchy *et al.*, "Establishing synthesis–composition–property relationships for enhanced and reproducible thermoelectric properties of MgAgSb," *Journal of Materials Chemistry A,* 10.1039/D2TA05936C vol. 10, no. 40, pp. 21716-21726, 2022, doi: 10.1039/D2TA05936C.

[32] El-Genk MS, Saber HH, Caillat T, Sakamoto J. Tests results and performance comparisons of coated and un-coated skutterudite based segmented unicouples. Energ Conver Manage 2006;47(2):174–200. https://doi.org/10.1016/j.enconman.2005.03.023.

[33] Saber HH, El-Genk MS, Caillat T. Tests results of skutterudite based thermoelectric unicouples. Energ Conver Manage 2007;48(2):555–67. https://doi.org/10.1016/j.enconman.2006.06.008.

[34] C. E. Whiting, "Empirical Performance Analysis of MMRTG Power Production and Decay," in *2020 IEEE Aerospace Conference*, 7-14 March 2020 2020, pp. 1-9, doi: 10.1109/AERO47225.2020.9172270.

[35] R. Mesalam *et al.*, "Impedance spectroscopy characterization of neutron irradiated thermoelectric modules for space nuclear power," *AIP Advances,* vol. 9, no. 5, 2019, doi: 10.1063/1.5095619.

[36] C. Barklay, D. Kramer, C. Whiting, R. Ambrosi, and R. Mesalam, "Concept for a Cascaded Multi-Mission Radioisotope Thermoelectric Generator," in *2020 IEEE Aerospace Conference*, 7-14 March 2020 2020, pp. 1-7, doi: 10.1109/AERO47225.2020.9172602.

[37] C. E. Whiting, R. M. Hoffman, C. D. Barklay, and P. C. Schmitz, "Low Thermal Loading and Operational Voltage Limits as Methods for Enabling MMRTG as a Power Source for Lunar Missions," in *2021 IEEE Aerospace Conference (50100)*, 6-13 March 2021 2021, pp. 1-9, doi: 10.1109/AERO50100.2021.9438297.

[38] A. Barco *et al.*, "Design and Development of the ESA Am-Fueled Radioisotope Power Systems," in *2019 IEEE Aerospace Conference*, 2-9 March 2019 2019, pp. 1-11, doi: 10.1109/AERO.2019.8741786.

[39] Tailin L, et al. Comprehensive modeling and characterization of Chang'E-4 radioisotope thermoelectric generator for lunar mission. Appl Energy 2023;336: 120865. https://doi.org/10.1016/j.apenergy.2023.120865.

[40] Liu Y, Zhang Y, Xiang Q, Hao F, An Q, Chen H. Comprehensive modeling and parametric analysis of multi-mission radioisotope thermoelectric generator. Appl Therm Eng 2023;219:119447. https://doi.org/10.1016/j.applthermaleng.2022.119447.

[41] Kim HS, Kikuchi K, Itoh T, Iida T, Taya M. Design of segmented thermoelectric generator based on cost-effective and light-weight thermoelectric alloys. Mater Sci Eng B 2014;185:45–52. https://doi.org/10.1016/j.mseb.2014.02.005.

[42] J. Camut, E. Müller, and J. de Boor, "Analyzing the Performance of Thermoelectric Generators with Inhomogeneous Legs: Coupled Material–Device Modelling for Mg2X-Based TEG Prototypes," *Energies*, vol. 16, no. 9, doi: 10.3390/en16093666.

[43] Camut J, Ziolkowski P, Ponnusamy P, Stiewe C, Mueller E, de Boor J. Efficiency measurement and modeling of a high-performance Mg2(Si,Sn)-based Thermoelectric generator. Adv Eng Mater 2023;:25(1):2200776. https://doi.org/10.1002/adem.202200776.

[44] Martinez A. Resistance-capacitance thermal models as alternatives to finite-element numerical models in the simulation of thermoelectric modules for electric power generation. Energ Conver Manage 2023;292:117419. https://doi.org/10.1016/j.enconman.2023.117419.

[45] P. Ying *et al.*, "A robust thermoelectric module based on MgAgSb/Mg3(Sb,Bi)2 with a conversion efficiency of 8.5% and a maximum cooling of 72 K," *Energy & Environmental Science,* 10.1039/D2EE00883A vol. 15, no. 6, pp. 2557-2566, 2022, doi: 10.1039/D2EE00883A.

[46] Wilbrecht S, Beitelschmidt M. The potential of a cascaded TEG system for waste heat usage in railway Vehicles. J Electron Mater 2018;47(6):3358–69. https://doi.org/10.1007/s11664-018-6094-z.

[47] Lamba R, Manikandan S, Kaushik SC. Performance analysis and optimization of concentrating solar thermoelectric generator. J Electron Mater 2018;:47(9): 5310–20. https://doi.org/10.1007/s11664-018-6410-7.

[48] Zhao B, Pei G, Raman AP. Modeling and optimization of radiative cooling based thermoelectric generators. Appl Phys Lett 2020;117(16):163903. https://doi.org/10.1063/5.0022667.

[49] Jing H, et al. A skutterudite thermoelectric module with high aspect ratio applied to milliwatt radioisotope thermoelectric generator. Appl Energy 2023;350:121776. https://doi.org/10.1016/j.apenergy.2023.121776.

[50] L. Gard and A. Lane, "Status of Current Aerojet Rocketdyne RPS Programs," in *2024 IEEE Aerospace Conference*, 2-9 March 2024 2024, pp. 1-11, doi: 10.1109/AERO5975.2024.10521094.

[51] Richard M. Ambrosi *et al.*, "The European Radioisotope Power Systems Program: Updates & Synergies," presented at the Nuclear and Emerging Technologies for Space (NETS 2024) Santa Fe, NM, US, 6-10 May 2024, 2023.

[52] Ramy Mesalam *et al.*, "Am-241 Powered Dynamic Radioisotope Power System (DRPS) for Long Duration Lunar Rovers," presented at the European Space Power Conference Elche, ES, 2-6 October 2023, 2023.

[53] European Space Agency (ESA), "Technology 2040: A vision for the European Space Agency," 2025.

[54] Li J, et al. Thermal and electrical analysis of SiGe thermoelectric unicouple filled with thermal insulation materials. Appl Therm Eng 2018;134:266–74. https://doi.org/10.1016/j.applthermaleng.2018.01.100.

[55] T. Hammel, R. Bennett, and B. Sievers, "Evolutionary upgrade for the multi-mission radioisotope thermoelectric generator (MMRTG)," in *2016 IEEE Aerospace Conference*, 5-12 March 2016 2016, pp. 1-8, doi: 10.1109/AERO.2016.7500748.

[56] Vigier J-F, et al. Optimization of uranium-doped americium oxide synthesis for space application. Inorg Chem 2018;57(8):4317–27. https://doi.org/10.1021/acs.inorgchem.7b03148.

[57] E. J. Watkinson *et al.*, "Thermal Properties and Behaviour of Am-Bearing Fuel in European Space Radioisotope Power Systems," *Thermo*, vol. 1, no. 3, pp. 297-331doi: 10.3390/thermo1030020.

[58] C. Gong and B. J. Hardy, "Power distribution for an Am/Cm bushing melter," United States, 1996. [Online]. Available: http://inis.iaea.org/search/search.aspx?orig_q=RN:29006849.

[59] Mersen Scotland Holytown Ltd, "PROPERTIES OF CALCARB®- RIGID CARBON INSULATION CBCF 18-2000," ed, 2009.

[60] Lacoste M, Lacombe A, Joyez P, Ellis RA, Lee JC, Payne FM. Carbon/carbon extendible nozzles. Acta Astronaut 2002;50(6):357–67. https://doi.org/10.1016/S0094-5765(01)00178-3.

[61] Materion Corporation, "AlBeMet® Property Datasheet," ed.

[62] Matula RA. Electrical resistivity of copper, gold, palladium, and silver. J Phys Chem Ref Data 1979;8(4):1147–298. https://doi.org/10.1063/1.555614.

[63] B. Zhu *et al.*, "Realizing record high performance in n-type Bi2Te3-based thermoelectric materials," *Energy & Environmental Science*, 10.1039/D0EE01349H vol. 13, no. 7, pp. 2106-2114, 2020, doi: 10.1039/D0EE01349H.

[64] Kim KT, Ha GH. Fabrication and Enhanced thermoelectric properties of alumina nanoparticle-dispersed Bi0.5Sb1.5Te3 matrix composites. J Nanomater 2013,;2013 (1):821657. https://doi.org/10.1155/2013/821657.

[65] W. W. Schultz, "The chemistry of americium," Energy Research and Development Administration (ERDA) critical review series, 1976.

[66] Yamada Y, Sakate H, Sakuma F, Ono A. High-temperature fixed points in the range 1150 °C to 2500 °C using metal-carbon eutectics. Metrologia 2001,;38(3):213. https://doi.org/10.1088/0026-1394/38/3/3.

[67] R. E. Tate, "Light weight radioisotope heater unit (LWRHU): a technical description of the reference design," Los Alamos National Lab., NM (USA), United States, 1981. [Online]. Available: https://www.osti.gov/biblio/5253319.

[68] H. Inouye, C. T. Liu, and R. G. Donnelly, "NEW PLATINUM-RHODIUM-TUNGSTEN ALLOYS FOR SPACE ISOTOPIC HEAT SOURCES," OAK RIDGE NATIONAL LABORATORY, 1972.

[69] Wen C-D, Mudawar I. Modeling the effects of surface roughness on the emissivity of aluminum alloys. Int J Heat Mass Transf 2006;49(23):4279–89. https://doi.org/10.1016/j.ijheatmasstransfer.2006.04.037.

[70] C. J. e. a. Smithells, "Radiating properties of metals," in *Metals Reference Book (Fifth Edition)*, C. J. Smithells Ed.: Butterworth-Heinemann, 1976, pp. 1014-1025.

[71] J. H. Henninger, "Solar absorptance and thermal emittance of some common spacecraft thermal-control coatings," 1984.

[72] G. H. Heiken, D. T. Vaniman, and B. M. French, *Lunar Sourcebook, A User's Guide to the Moon*. 1991.

[73] K. Zabrocki, C. Goupil, H. Ouerdane, Y. Apertet, W. Seifert, and E. Müller, "Continuum Theory of TE Elements," in *Continuum Theory andModeling of Thermoelectric Elements*, 2016, pp. 75–156.

[74] Wang S, Xie T, Xie H. Experimental study of the effects of the thermal contact resistance on the performance of thermoelectric generator. Appl Therm Eng 2018; 130:847–53. https://doi.org/10.1016/j.applthermaleng.2017.11.036.

[75] Beltrán-Pitarch B, Vidan F, García-Cañadas J. Thermal contact resistance evaluation of a thermoelectric system by means of three I-V curves. Int J Heat Mass Transf 2021;173:121247. https://doi.org/10.1016/j.ijheatmasstransfer.2021.121247.

[76] Ponnusamy P, de Boor J, Müller E. Using the constant properties model for accurate performance estimation of thermoelectric generator elements. Appl Energy 2020;262:114587. https://doi.org/10.1016/j.apenergy.2020.114587.

[77] T. V. Mathew, "Genetic algorithm," Report submitted at IIT Bombay, 2012.

[78] Hamdia KM, Zhuang X, Rabczuk T. An efficient optimization approach for designing machine learning models based on genetic algorithm. Neural Comput Appl 2021;33(6):1923–33. https://doi.org/10.1007/s00521-020-05035-x.

[79] Al Malki MM, Shi X, Qiu P, Snyder GJ, Dunand DC. Creep behavior and post-creep thermoelectric performance of the n-type skutterudite alloy Yb0.3Co4Sb12. J Materiomics 2021;7(1):89–97. https://doi.org/10.1016/j.jmat.2020.07.012.

[80] Al Malki MM, Snyder GJ, Dunand DC. Mechanical behaviour of thermoelectric materials – a perspective. Int Mater Rev 2023;68(8):1050–74. https://doi.org/10.1080/09506608.2023.2193785.

[81] Male JP, Hogan B, Wood M, Cheikh D, Snyder GJ, Bux SK. Using vacancies to tune mechanical and elastic properties in La3−xTe4, Nd3−xTe4, and Pr3−xTe4 rare earth telluride thermoelectric materials. Mater Today Phys 2023;32:101016. https://doi.org/10.1016/j.mtphys.2023.101016.

[82] J.-P. Fleurial, S. Bux, and T. Caillat, "Engineering of Novel Thermoelectric Materials and Devices for Next Generation, Long Life, 20% Efficient Space Power Systems," in *11th International Energy Conversion Engineering Conference*, (Joint Propulsion Conferences: American Institute of Aeronautics and Astronautics, 2013.

[83] Williams HR, Ambrosi RM, Bannister NP, Samara-Ratna P, Sykes J. A conceptual spacecraft radioisotope thermoelectric and heating unit (RTHU). Int J Energy Res 2012;36(12):1192–200. https://doi.org/10.1002/er.1864.

[84] Karri NK, Mo C. Structural reliability evaluation of thermoelectric generator modules: influence of end conditions, leg geometry, metallization, and processing temperatures. J Electron Mater 2018;47(10):6101–20. https://doi.org/10.1007/s11664-018-6505-1.

[85] Bao X, et al. Mechanical properties of thermoelectric generators. J Mater Sci Technol 2023;148:64–74. https://doi.org/10.1016/j.jmst.2022.10.081.

[86] Erturun U, Erermis K, Mossi K. Effect of various leg geometries on thermo-mechanical and power generation performance of thermoelectric devices. Appl Therm Eng 2014;73(1):128–41. https://doi.org/10.1016/j.applthermaleng.2014.07.027.

[87] Turenne S, Clin T, Vasilevskiy D, Masut RA. Finite element thermomechanical modeling of large area thermoelectric generators based on bismuth telluride alloys. J Electron Mater 2010;39(9):1926–33. https://doi.org/10.1007/s11664-009-1049-z.

[88] Stevens JW. Optimal design of small ΔT thermoelectric generation systems. Energ Conver Manage 2001;42(6):709–20. https://doi.org/10.1016/S0196-8904(00)00099-6.

[89] Lee CH, Caillat T, Pinkowski S. Bayesian reliability analysis of the enhanced multimission radioisotope thermoelectric generator. J Spacecr Rocket 2024;61(2): 557–69. https://doi.org/10.2514/1.A35785.

[90] Liu Y, et al. Mechanical test of thermoelectric device in RTG prototype. J Phys Conf Ser 2021,;1865(3):032080. https://doi.org/10.1088/1742-6596/1865/3/032080.

[91] Vasavada AR. Mission overview and scientific contributions from the mars science laboratory curiosity rover after eight years of surface operations. Space Sci Rev 2022;218(3):14. https://doi.org/10.1007/s11214-022-00882-7.

[92] R. Welch, D. Limonadi, and R. Manning, "Systems engineering the Curiosity Rover: A retrospective," in *2013 8th International Conference on System of Systems Engineering*, 2-6 June 2013 2013, pp. 70-75, doi: 10.1109/SYSoSE.2013.6575245.

[93] Steven Oleson *et al.*, "Dynamic Radioisotope Power System (DRPS) Design Reference Mission (DRM) Lunar Rover," 2022.